EFFECTS OF CONTACT GEOMETRY ON THE TRIBOLOGICAL EVALUATION OF GREASE

A Dissertation

by

CARLOS JOEL SANCHEZ

Submitted to the Office of Graduate and Professional Studies of
Texas A&M University
in partial fulfillment of the requirements for the degree of

DOCTOR OF PHILOSOPHY

Chair of Committee,	Hong Liang
Committee Members,	Jun Zou
	Sai Lau
	Partha Muhkerjee
Head of Department,	Andreas A Polycarpou

December 2016

Major Subject: Mechanical Engineering

Copyright 2016 Carlos Joel Sanchez

ABSTRACT

This research investigates the influence of morphological characteristics on tribological performance of lubricating grease. The use of grease as a semi-solid lubricant has been well established in reducing friction and improving overall performance of moving parts in mechanical systems. Tribological evaluation has been tailored to specific applications individually such that the fundamental understanding has not be achieved as much as oils. This research aims to establish a more consistent methodology to evaluate any type of grease and obtain an understanding in the influence of morphological characteristics on tribological performance. New experimental approaches were used to support this research. This includes grease formulation, and tribotesting using various methodologies to evaluate the performance of grease. Unique testing apparatuses and procedures were developed to reveal insight into lubricating performance.

Tribotests were designed and evaluated against various contact configurations. Contacts of point, line, and area were comparatively studied. In this research, four grease formulations were investigated using three different contact geometries. The formulations included an industry standard compound, and a base petroleum grease. Analysis of tribotest results showed that the frictional performance follow a similar trend despite their contact configurations. Using a contact factor, those tests could be unified and compared directly. In addition, an in situ approach reveals that a shear stress could be effectively support dispersion of additives in grease. Gaining a better understanding

of the lubricating behavior of grease will contribute to the development of more efficient grease formulations, and allow for more accurate recommendations for grease lubricating practices.

This research has significance for industries and applications where grease lubrication is critical; such as oil and gas, automotive, aerospace, and general bearing applications. Greases used in the oil and gas industry for example contain numerous additives. One primary concern is the homogenization of a grease mixture. Since grease consist of many individual components, they will have a tendency to separate and produce inconsistent. These grease compounds must be able to perform well under high contact pressures and at high temperatures for deep well drilling. Situations such as these pose many challenges in regards to the testing equipment used to evaluate them, as well as computational methods used to analyze the resultant data.

DEDICATION

To my family and my wife, who supported me though all these years.

ACKNOWLEDGEMENTS

I would like to thank my advisor and committee chair, Dr. Hong Liang for all her support and guidance throughout the course of my graduate career. I gained invaluable knowledge and experience through her support that I will carry with me for the rest of my life. I would also like to thank my committee members, Dr. Jun Zou, Dr. Sai Lau and Dr. Partha Muhkerjee or their support. I am also grateful for the support I received through the American Petroleum Institute, and all the members who served as mentors in my grease testing.

I am extremely grateful to my parents, Carlos and Bertha Sanchez, for all of their support throughout my academic career. They have made a lot of sacrifices throughout the years to send me to Texas A&M so that I may realize my dream of earning a PhD. I would not be where I am without them.

I would especially like to thank my current fiancé and future wife, Leia Lozano, for staying by my side and supporting me all my years in graduate school.

CONTRIBUTORS AND FUNDING SOURCES

Contributors

This work was supervised by a dissertation committee consisting of Dr. Hong Liang (advisor and chair) and Dr. Sai Lau (member) and Dr. Partha Mukherjee (member) of the Mechanical Engineering Department and Dr. Jun Zou (member) of the Electrical and Computer engineering department.

The testing apparatus described in Chapter III was supported by the American Petroleum Institute (API). Test samples were proved through API Workgroup 1066. The data analysis described in Chapter V was supervised by the scientists at

All work for the thesis (or) dissertation was completed by the student, under the advisement of Dr. Hong Liang of the Department of Mechanical Engineering.

Funding Sources

Graduate study was supported by the Texas A&M University Turbomachinery Research Laboratory, The American Petroleum Institute, and Shell Global Technologies.

NOMENCLATURE

API	American Petroleum Institute
HTT	High Temperature Tribometer
COF	Coefficient of Friction
LBNL	Lawrence Berkeley National Laboratory
ALS	Advanced Light Source
ASTM	American Society for Testing and Materials
CT	Computed Tomography
µCT	Micro Computed Tomography
FF	Friction Factor
RPM	Revolutions per Minute
FeO	Iron Oxide
ZrP	Zirconium Phosphate
PJ	Petroleum Jelly
MU	Make-up
BO	Break-out

TABLE OF CONTENTS

Page

ABSTRACT ii

DEDICATION iv

ACKNOWLEDGEMENTS v

CONTRIBUTORS AND FUNDING SOURCES vi

NOMENCLATURE vii

TABLE OF CONTENTS viii

LIST OF FIGURES x

LIST OF TABLES xiv

CHAPTER I INTRODUCTION 1

1.1 A brief background on tribology 1
1.2 Roles of lubrication 4
1.3 Current practices in grease testing 9

CHAPTER II MOTIVATION AND OBJECTIVES 15

CHAPTER III ZERO AND ONE DIMENSIONAL CONTACT 17

3.1 Tribotesting apparatus 17
3.2 Point contact 21
3.3 Line contact 27
3.4 Environmental conditions 34
3.5 Results of tribotesting 36

CHAPTER IV TWO DIMENSIONAL CONTACT 41

4.1 Design strategy and configuration for grease evaluation 41
4.2 Calculations and data analysis 50
4.3 Grease additive evaluation 57

4.4 Data analysis and discussion 66
4.5 Surface analysis 68

CHAPTER V EFFECTS OF GEOMETRIC FACTORS OF FRICTION 70

5.1 Contact geometry 70
5.2 Geometric analysis 75

CHAPTER VI DIRECT PROBING OF LUBRICANTS 82

6.1 Experimental design and configuration 82
6.2 Digital imaging and tomography approach 84
6.3 Feasibility of tomography 86
6.4 Viscometer device for tomography 90
6.5 Synchrotron micro tomography 98
6.6 Tomography results and discussion 99
6.7 Significance of *in situ* results 105

CHAPTER VII CONCLUSIONS AND FUTURE RECOMMENDATIONS 107

7.1 Conclusions 107
7.2 Future recommendations 107

REFERENCES 109

LIST OF FIGURES

Page

Figure 1. Typical Stribeck Curve for lubricated sliding surfaces [19]. 5

Figure 2. Diagram of the standard components that makeup lubricating grease. 8

Figure 3. Schematic diagram of a standard four ball tribometer. 12

Figure 4. Schematic diagram of a typical pin-on-disc tribometer configuration. 18

Figure 5. Image of the high temperature tribometer (HTT) apparatus used in this research. 20

Figure 6. Schematic diagram of a ball on disc contacting surfaces with the resulting Hertzan contact geometry and stress locations. 23

Figure 7. Diagram of the new channel and ball friction test setup for grease evaluation. 28

Figure 8. (a) Disc shaped insert with a 0.25inch race channel, and (b) Pin with a 0.25inch bearing ball and collar welded in place. 29

Figure 9. Schematic diagram of the two dimensional ball in channel contact. 30

Figure 10. Schematic diagram of the geometric parameters of the contacting materials. 31

Figure 11. High temperature tribometer (HTT) modified to accept liquid nitrogen for low temperature experiments. 35

Figure 12. Plot of friction coefficient versus temperature for all four grease groups under sliding point contact geometry. 38

Figure 13. Plot of friction coefficient versus temperature for all four grease groups under sliding point contact geometry. 39

Figure 14. (a) Cross sectional view of a typical threaded connection for tubing and casing joints; and (b) Close up view of the mating threads coated in thread compound. 42

Figure 15. Examples of galling damage on tubing threads and on a flat disc shaped metal specimen. 43

Figure 16. (a) Diagram of the major components of the standard API 7A1 machine used for evaluating thread compounds; and (b) Drawing of a standard 1 inch bolt used for the tests. 44

Figure 17. New load cell assembly that was integrated into the original API 7A1 machine. 46

Figure 18. (a) Image of the new ring shaped test specimens; and (b) Diagram of how the specimens fit into the new load cell assembly, illustrating the dynamic (left) and stationary (right) specimens. 47

Figure 19. (a) A tests specimen pair with an even coating of grease applied; and (b) The coated tests specimens loaded into the machine for testing. 49

Figure 20. Diagram of the new configuration meant to evaluate the frictional performance of grease. 50

Figure 21. Diagram of the forces acting on the ring specimen and the bolt threads, as well as important dimensions under consideration. 51

Figure 22. Typical Make-Up and Break-Out torque, and load versus rotation plot of a standard grease compound. 55

Figure 23. Plot of the calculated friction coefficient versus the rotation. 56

Figure 24. Plot of friction coefficient versus rotation for a grease of varied additive composition. 57

Figure 25. The (b) Zygo interferometer and (a) Keyance optical microscope used to evaluate the surface of the metal test specimens, with examples of their respective resulting images. 68

Figure 26. View of a test specimen surface after a friction experiment performed using the NCS30 grease group. 69

Figure 27. Schematic diagrams showing (a) point (0D) contact, (b) line (1D) contact, and (c) area (2D) contact geometry. 71

Figure 28.Schematic diagrams of the three primary lubrication regimes represented by a Stibeck Curve analysis. 73

Figure 29. Schematic diagram of the three contact geometries used in this research, along with the corresponding geometric parameter, K. 76

Figure 30. Plot of pressure distribution at constant load versus effective contact area. 79

Figure 31.Plot of friction coefficient versus contact geometry type for the four grease groups under investigation. 80

Figure 32. Diagram of the procedure and basic components of a medical CT scan. 84

Figure 33. Complete three dimensional reconstruction of the Discoid cockroach. (a) The full roach showing the outline of the plastic tube and capillary wax at the bottom. (b) The full roach made more translucent, with the AG NPs superimposed within the body. 88

Figure 34. Close up views of the AG NPs (in red) within the cockroach body. (a) View of the right side of the body, showing the top thoracic segments. (b) Front view of the top thoracic segments with NPs superimposed. 89

Figure 35. The concentric tubes for shearing grease. (a) Diametric view and (b) Section view of the tubes. The grease samples were deposited within the gap between the tubes (red arrow). The curved arrow indicates the rotation direction. 91

Figure 36. Diagram of the concentric cylinder testing rig used to shear the grease/nanoparticle mixture. 93

Figure 37. (a) Side view of the testing rig, indicating the axis or rotation, and (b) Top view of the concentric cylinders with grease/additive mixture, illustrating the scanning configuration. 94

Figure 38. Diagram view of the concentric cylinder testing rig, indicating key parameters in cylindrical coordinates. 95

Figure 39. Plot of the mass attenuation coefficient for zirconium (Zr) and carbon (C). The values for all elements were derived from the National Institute of Standards and Technology (NIST) database for X-Ray attenuation. 100

Figure 40. The absorption coefficient distribution of datasets. 101

Figure 41. The top view of 3D visualization for group 2 built by 18.2 keV datasets (a) before rotation, (b) after rotation. (c-d) The side sectional view corresponding to the (a-b). The distribution of α-ZrP additives (e) before rotation and (f) after rotation. The box size is 1.7x3.3x1.5 mm. 103

Figure 42. Visual representation of the behavior of the α-ZrP nanoparticles (a) as received, and (b) after a shear stress is applied to the system. 104

LIST OF TABLES

Page

Table 1. Standard grease tests procedures typically performed by grease manufacturers. 10

Table 2. Material properties with resultant Hertian contact values. 26

Table 3. Summary of the radii for the ball, channel indentation, and channel track. All dimensions in inches. 31

Table 4. Results of a Hertxian contact analysis of the two mating materials. 34

Table 5. List of all grease sample test groups. 36

Table 6.Average coefficients of friction of each grease group for point contact at various temperatures. 37

Table 7. Average coefficients of friction of each grease group for line contact at various temperatures. 37

Table 8. List of grease sample test groups. 60

Table 9. Summary of the data collected for a complete torque test of Group 1, NCS-30 reference compound. 61

Table 10. Summary of the data collected for a complete torque test of Group 2, NCS-30 + 2.3wt% Fe3O4. 62

Table 11. Summary of the data collected for a complete torque test of Group 3, petroleum jelly. 63

Table 12. Summary of the data collected for a complete torque test of Group 4, petroleum jelly + 2.3wt% a-ZrP. 64

Table 13. Summary of the calculated slopes for each data set and the calculated friction factor for each group. 66

Table 14.Summary of the three contact regions experienced by the tribotesting methods discussed in this research, along with the corresponding governing parameters and resultant contact area. 77

CHAPTER I

INTRODUCTION

This chapter provides background information regarding the thesis topic of grease formulation, testing, and characterization. The role of additives in grease will also be discussed.

1.1 A brief background on tribology

The field of tribology aims to better understand surfaces that slide and move in relative motion with one another. One of the key aspects of this discipline is to understand and improve the frictional performance of these moving parts by analyzing their frictional behavior. It focuses on three interdisciplinary sciences of the interacting materials: friction; lubrication; and wear. The term "tribology" stems from the Greek phrase "tribos," which means to rub, and was coined in 1967 Europe by the Organization for Economic and Cooperation and Development [1]. Although it is a relatively new scientific discipline, the principles of tribology are ever present in today's world, with a constant demand to improve the efficiency of everyday systems. Automobiles, such as cars and trucks, for example waste an average of one third of fuel consumed due to frictional losses in the engine, transmission, tires, and other auxiliary systems [2, 3]. The ability to understand and improve upon the way material interact in simple and complex systems will lead to advancements in numerous fields.

Some of the earliest concepts of applied tribology can be seen through antiquity when our human ancestors first began to create fire through the rubbing of sticks.

Research in paleontology has shown that ancient people would also create fire by striking flint stones together [1]. Early people would essentially take advantage of the friction performance of various materials to generate heat. In addition to creating friction, historians have shown that ancient people used several methods to reduce it. Many early lubricating practices utilized natural materials such as animal or plant oils to help reduce friction. Once such accord can be traced to 3500 B/C/ in ancient Sumerian culture, where people would use animal fat substance to lubricate the axles of their wheels [1]. Although the methods were crude, the importance of friction and lubrication began to be established.

The earliest records of friction studies as a science can be traced to Leonardo Da Vinci in the 15th century. Da Vinci recognized friction as a force that opposed the motion of an object and developed several experiments to demonstrate its effects [4]. In one experiment, Da Vinci placed a wooden block on an inclined plane. By lifting the plane at different angles, Da Vinci took note when the block would begin to slide. In another, he attached weights to a block sitting on a flat surface to measure how much weight was required to begin sliding. Through his experiments, Da Vinci was able to prove that an objects' weight is directly proportional to its resistance to friction. This postulation is what we recognize today as the coefficient of friction, a non-dimensional proportionality constant.

While Da Vinci set the groundwork for the study of friction, the study of tribology did not fully come into existence until the late 17th century with the works of Guillaume Amontons, a French physicist. Known as the father of tribology, Amontons

reinvigorated the study of friction set forth by Da Vinci, performing his own experiments and developing two key laws of friction: 1.The resistive force of friction is directly proportional to the load being applied; and 2. The force of friction is not dependent of apparent contact area [5]. While these laws are widely known and understood in the field of tribology, they become invalid in many practical situations [6]. For instance, when a lubricant is introduced between sliding surfaces the effects of the applied load become reduced. However, the influence of these early works are clearly prevalent in present day tribological studies.

As mentioned above, lubrication can greatly affect frictional performance and requires a different understanding to better evaluate it. One of the greatest impacts of tribological study is in regards to the wearing of the mating materials. Wear is described as a loss of material as a direct result of friction. The loss of material is a critical issue that can greatly affect the performance of countless mechanical systems. An understanding of wear mechanisms is needed to reduce friction and improve efficiency. One of the most common methods to reduce wear is through the introduction of a lubricant to the interacting materials; hereby referred to as a tribosystem. A well lubricated tribosystem has been shown to reduce friction and minimize wear by creating a protective barrier in between the rubbing materials. However, the type of lubricant becomes of great interest as different lubricants will have varied performance under certain conditions. The testing and analysis of various lubricants will be discussed in later sections.

1.2 Roles of lubrication

The purpose of lubrication is to introduce a protective film of material in between two or more interacting surfaces to reduce the effects of friction. Having a lubricant present in between the moving surfaces, the wear and thermal energy may also be reduced. In addition, lubricants can serve as a means to remove wear debris from the system, thereby improving the sliding performance and preventing hard particle debris from causing abrasive damage. A common method of improving system performance and efficiency is though lubrication. Lubricant types can be generally classified as being either solid, liquid, or gaseous [7]. Solid lubricants typically come in the form of a coating that is deposited onto one or both surfaces through a chemical or physical process [7, 8]. Gaseous lubricants aim to separate the mating surfaces with an insulating layer of flowing gas that may also serve to improve thermal performance [9]. In general, lubricants will often come in the form of liquids, such as oils or other fluids. The most common type of lubricant for mechanical gears and bearings is grease. Grease is not classified as a liquid lubricant, but as a semi-solid [10]. However, nearly all methods of grease analysis and characterization involve treating it as behaving like an oil [7, 11-13]. This tendency has been recognized as problematic in certain situations and new and ongoing research has been devoted to solving this issue [10, 14-16]. A better understanding of the tribological behavior of grease is needed.

The laws of friction as stated by Amontons are only applicable in certain situations, in particular dry sliding conditions; i.e. non-lubricated. The most prevalent method of characterizing the frictional properties between sliding, lubricated surfaces

revolves around the establishment of a “Stribeck Curve” for the given lubricant. Developed by Richard Stribeck in 1901 as a result of performing numerous experiments on oil lubricated journal bearings, the curve can be used to distinguish between various lubrication regimes among mating surfaces in sliding contact [17, 18]. A typical Stribeck Curve for oil lubricated mating surfaces can be seen in Figure 1.

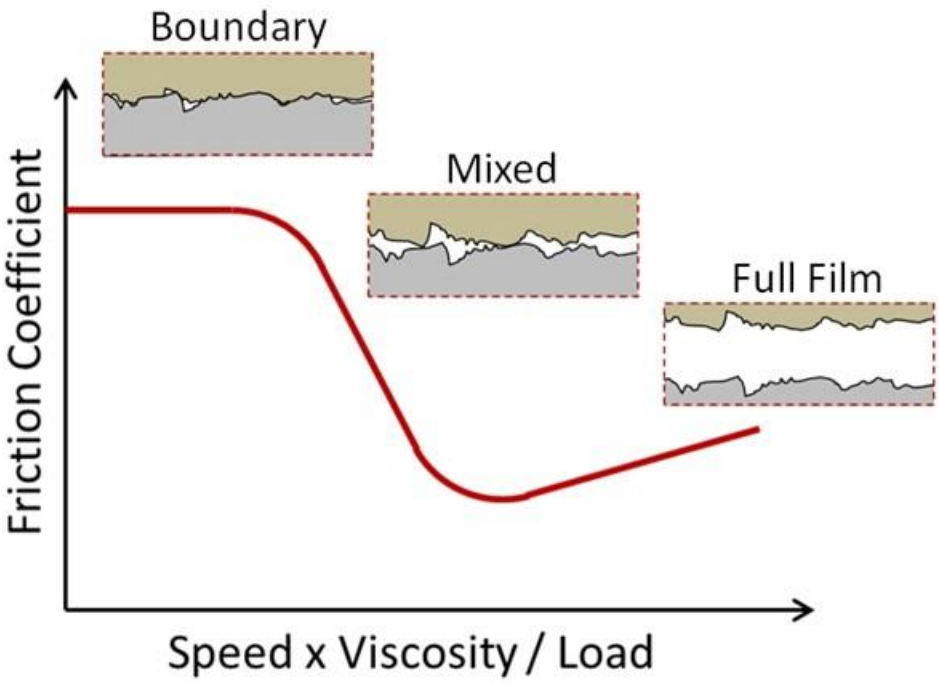

Figure 1. Typical Stribeck Curve for lubricated sliding surfaces [19].

The curve displays the relationship between the coefficient of friction, and a dimensionless parameter referred to as the Stribeck Number, S. The Stribeck Number is commonly represented by the following equation:

$$\boldsymbol{S} = \frac{V * \eta}{F}$$

Equation 1.1

where V is the sliding speed of the materials, η is the viscosity of the fluid, and F is the applied load. The Stribeck curve illustrates three very distinct lubrication regimes: boundary, mixed, and hydrodynamic full film. Boundary lubrication occurs at low speeds and viscosity, and high loads, resulting in surface to surface contact of the mating parts. Here, the friction is relatively high, and the oil only provides superficial lubrication within the surface asperities; just enough lubricant exist to prevent dry friction to occur. As the speed and viscosity are increased, and load decreased, the mating surfaces will begin to separate to the point where a fully developed layer of lubricant separates them. This regime is referred to as hydrodynamic lubrication. In between the boundary regime and hydrodynamic regime is the mixed lubrication regime wherein the surfaces are partially in contact and partially separated by lubricant.

Although three distinct lubrication regimes can be established in relation to speed, viscosity, and load, many cases exist where mechanical components will operate in one ore of more of the regimes. A Stribeck Curve can essentially be used as means for

comparing the modeled tribological behavior seen in the plot, versus that of the real world application.

The most common lubrication theory for grease revolves around the regime that exists between mixed and hydrodynamic, known as the elastohydrodynamic lubrication (EHL) regime [10, 15, 19, 20]. This theory is often applied to grease lubricated ball bearings that operate in conditions where the bearing balls will tend to “float” on a bed of grease in some instances, and contact the race channel in another [21]. However, conventional EHL modeling is flawed for cases where mating parts often reach or come close to the boundary lubrication regime. Many roller bearings have been documented to operate below the EHL regime, approaching boundary lubrication [22, 23]. For conditions where lubrication between mating marts is significantly low it becomes difficult to analyze and accurately predict grease performance. In order to still apply EHL models to the grease system, it is often assumed that a thin lubricating film exists as a result of base oils escaping the grease matrix [24]. This assumption is problematic as it greatly depends on the grease formulation and the test conditions. Of concern is the environmental temperature, and/or temperature fluctuations developed through friction. Therefore, a better method for modeling grease is needed that will more accurately represent what is occurring at the contact region. Better classification and testing methodologies for grease are desired.

Lubricating greases are classified as semi-solid or semi-fluid mixtures of thickening agents and liquid lubricants [25]. Due to their consistency, greases are often used in enclosed areas where constant lubrication is needed, such as bearing housings

and gear boxes. Grease can be broken up into three main components: a base oil, a thickener, and additives of various types. The standard breakdown of lubricating grease can be seen in **Figure 2**.

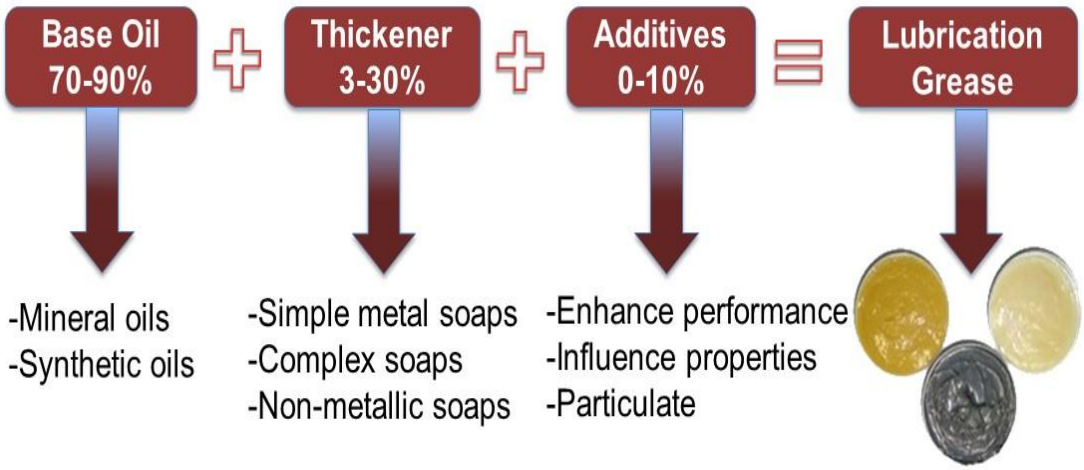

Figure 2. Diagram of the standard components that makeup lubricating grease.

The species, size, and concentrations of these individual components will vary depending on the intended use of the grease. In general, the base oil will consist of some form of mineral or synthetic oil. A thickener in the form of a metallic or synthetic soap will serve to suspend the base oil into a semi-solid structure and provide additional properties to the entire lubricant. Additive concentrations will range from 0wt% to ~10wt% and typically serve to enhance certain properties of the grease [26]. Graphite powder additives, for example, provide an additional lubricating film for surfaces

operating under high temperatures [27]. Another common additive that has been widely studies is zinc dithiophosphate (ZDDP), which can greatly reduce wear. However a known issue with ZDDP is the breakdown of the soaps used to suspend the grease mixture after a shear force is applied [28]. Essentially, ZDDP will tend to tear through the fibrous structure after some amount of shearing, thereby reducing the integrity of the grease mixture. Friction may be reduced for a short period, but once the fibrous structure of the soap begins to separate, the friction will increase. It was also shown that different soap structures will vary in behavior at the presence of the same concentration of ZDDP additives. Since ZDDP will cause the components of a grease to separate, it is not an ideal candidate for a friction modifier. With a wide range of grease formulations available, there becomes a need to more consistently evaluate each type.

1.3 Current practices in grease testing

As mentioned before, the testing procedures for liquid lubricants versus that of semi-solid lubricant differ. Many methods exist in which to test and characterize grease. The most common ASTM standard test procedures used by grease manufacturers to classify their products are listed in Table 1.

Table 1. Standard grease tests procedures typically performed by grease manufacturers.

Test Name	Characteristic Measured	Standard
Four Ball Test	Wear resistance, shear stability	ASTM D2266
Cone Penetration	Viscosity	ASTM D217
Dropping Point	Temperature dependence	ASTM D566
Corrosion Prevention	Corrosion resistance	ASTM D1743
Oil Separation	Separation while in storage	ASTM D1742
Timken Method	Load carrying capacity	ASTM D2509
Water interaction	Water washout characteristics	ASTM D1264

The standard tests listed in Table 1 can provide information such as the grease viscosity, temperature resistance, water resistance, load carrying ability, and shear stability. Taking all these characteristics into account, properly selecting a grease for a specific application is possible. However, while in service, grease can exhibit different behavior than what was originally reported. Likewise, real world scenarios can cause lubricating greases to behave differently than in a laboratory setting.

Depending on the application, grease will begin to degrade over time. The primary mode of grease degradation is oxidation as a result of environmental factors, such as temperature [29]. Regardless of the application, grease has been well document to degrade to a point where it will need to be replaced in order to preserve the integrity of the system [11, 30, 31]. Liquid lubricants, such as oils, will suffer from the same problem [32]. However, liquid lubricants are much easier to monitor due to their fluidity [32]. Likewise, removing degraded oil from a system is relatively simple compared to removing grease. A common example is changing the oil in a car engine. As it degrades

grease will tend to get thicker, resulting in inconsistent shear performance. Depending on the severity, a grease may even form a solid film on the mating surfaces that will hinder performance[33]. Changing the grease in a gearbox, for example, is quite a laborious process as it requires the complete removal of the thick grease from all components.

Since lubricating greases tend to vary in consistency over time, it becomes desirable to analyze the grease during and after its service life. The primary issues in testing in-service or used grease are in the collection process and determining the point in the service life at which it is collected. Methods have been devolved that aim to alleviate these issues by artificially aging grease to various degradation levels [30, 34]. The artificially aged grease is then subjected to typical testing procedures to determine performance over a particular service life range. This test methodology can result in decent correlations in performance; however there is much room for improvement. A methodology is needed that better replicates the service conditions of the grease and more accurately simulates "aged" grease. An ideal situation would be an *in situ* tribotesting method that can analyze grease in real time.

Tribotesting can lead to a better understanding of grease lubrication as it is used in real working conditions. The aim of any given tribotest is to analyze the friction, wear, and lubrication behavior of a system under controlled conditions. A mating material pair in sliding motion, as well as an intermediary lubricant is referred to as a tribosystem. One of the most commonly used tribology apparatus is a pin-on-disc tribometer (ASTM G99), (Figure 4) [35]. For this test, a disc substrate is rotated against

a stationary pin that has an applied normal load. The motion of the disc will cause the pin to deflect. The deflection is measured by the machine as the friction force. This test methodology will be further elaborated in a later section. Based on the conditions of the test and the friction results collected, an understanding of the contact morphology and lubrication performance of the tribosystem may be obtained. At present, the most common methodology to analyze grease for tribological performance is a four ball wear test (ASTM D2266) [36, 37]. A schematic diagram of this tests is shown in Figure 3.

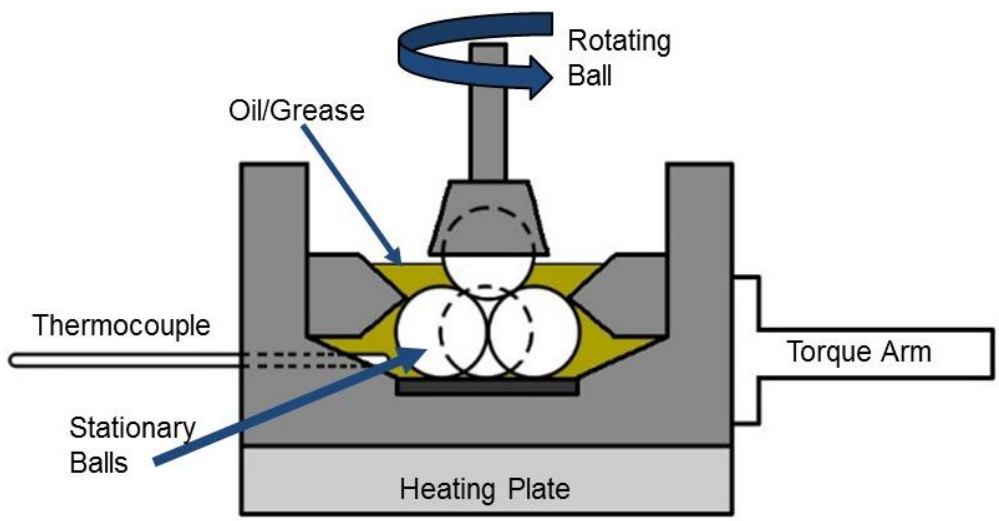

Figure 3. Schematic diagram of a standard four ball tribometer.

This test uses a ball bearing that is allowed to slide or rotate against three welded, stationary ball bearings. The single ball bearing is allowed to either roll or slide against the other three, while simultaneously applying a specified normal load. All four ball

bearings are housed inside an enclosure that is completely flooded with lubricating grease or oil. As the top ball rotates, the machine measures torque and normal load against speed and time, which is then used to calculate the coefficient of friction of the system. This test configuration allows for the mating materials to remain constantly lubricated with grease throughout the entire length of the test. Under other tribotest configurations, such as pin-on-disc, grease placed between the mating surfaces will have a tendency to be pushed out. Due to the consistency of lubricating grease, the mating surfaces will eventually cause it to be removed from the system entirely with no opportunity to be replenished. Over time, a pin-on-disc test that is lubricated with grease will achieve dry sliding conditions; at which point all data collected will be un-reliable.

Another common method to evaluate grease is to utilize a thrust bearing testing apparatus that is designed to conform to ASTM D3702 [12, 13, 38, 39]. For this type of test, a bearing is specifically designed to fit within a machine that simultaneously applies a normal load and rotates it at a set speed. Since the bearing has an enclosure, all grease applied will remain within the system for the duration of the test. Thrust bearing test configurations have been well documented to evaluate grease of varying consistency and environments [24, 39]. The key issue to consider with this type of test is the bearing geometry. In order to collect a used grease sample, the bearing must be disassembled, which is often difficult. The common solution is to collect the base oil that separates from the grease over the duration of the test [40, 41]. The separated oil is easily drained and collected for further analysis. While evaluating the separated oil may provide useful information, it will not provide a clear picture of the grease as a whole. An improved test

configuration is need that allows for the entirety of the used grease to be collected for analysis.

CHAPTER II

MOTIVATION AND OBJECTIVES

Lubricating greases are used extensively to improve the performance of countless mechanical systems. It has been shown that enhanced lubrication can lead to greater machine efficiency. However, despite their wide usage there does not exist a definitive methodology to analyze their performance. Unlike liquid lubricants such as oils, greases are highly specific to particular applications. Greases used in the oil and gas industry have very different properties than those intended for automotive use. Thus, the methodologies used to analyze them are varied and often require specialized equipment made to simulate the working conditions of the grease. Lubricating greases contain several components that must be mixed in a particular way. The separation of individual grease components, known as de-homoginization, is a leading cause of lubrication failure. Of note is distribution of additive particles within the grease. Evaluating the homogeneity of grease during testing and normal usage is difficult. The aim of this research will be to establish more effective tribotest procedures to evaluate grease to simulate real life conditions. The overall goal will be to identify geometrical factors affecting contact and tribological performance.

The primary objectives of this research will be the following:

1. Establishment of effective tribotest procedures to evaluate grease that correlates to real life working conditions.

2. Identification of geometrical factors affecting contact and tribological performance of grease.

3. Development of understanding in fundamentals of grease lubrication

The results of this research will contribute to the development of new lubricants. The new testing methodologies will be useful for the evaluation of new and existing grease compounds. Overall this research will contribute to a better understanding of grease lubrication and a better understanding of additive behavior.

CHAPTER III

ZERO AND ONE DIMENSIONAL CONTACT

This chapter will discuss point and line contact tribotest configuration. An analysis of the geometric relationships will be presented, as well as comparative friction results for each contact type.

3.1 Tribotesting apparatus

To evaluate the friction performance of various lubricating greases, a testing apparatus called a tribometer will be used. More specifically, a high temperature pin on disc type tribometer (HTT) will be employed for this research study. The pin on disc tribometer was manufactured my American Materials Testing Instruments (AMTI) in 1986, conforming to the stipulations set by the American Standards for Testing Materials (ASTM) G99 [35]. The testing apparatus consists of a stationary pin and a rotating disc, as depicted in Figure 4. The pin is placed under a set load against the rotating or oscillating disc. As the disc rotates, the pin will defect as a result of friction resistance forces. The higher the friction, the greater the deflection. The pin is fitted with load cells that measure the deflection as a resistance force that may be used in conjunction with the applied load to determine the coefficient of friction of both materials. Typically, the pin consist of a bearing ball that is affixed to a cylindrical shaft; hereby referred to as the pin assembly.

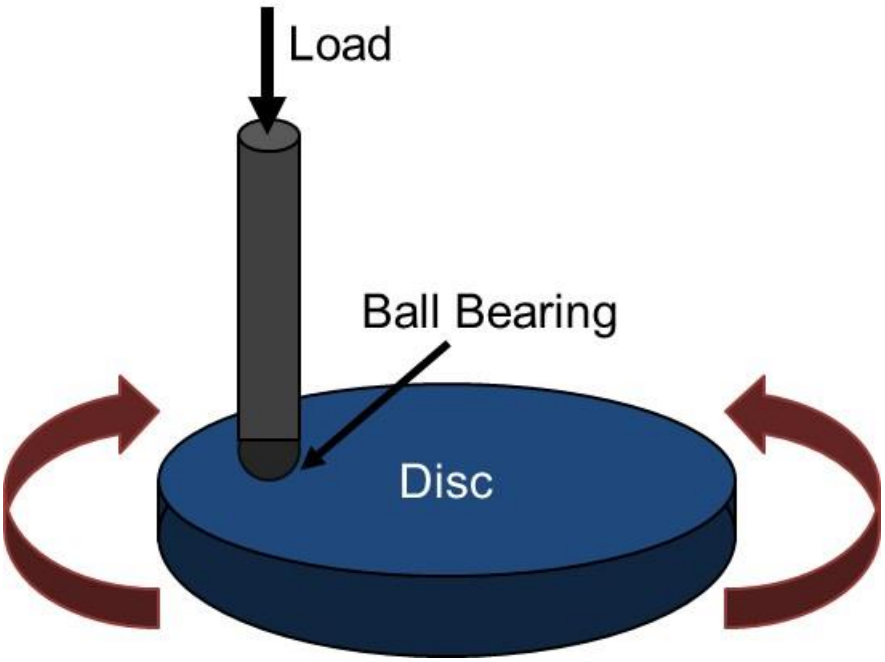

Figure 4. Schematic diagram of a typical pin-on-disc tribometer configuration.

The tribometer can be set to allow the disc to wither rotate or oscillate at various speeds and frequencies. For the current research, the samples will be evaluated using full rotation at 25 revolutions per minute (RPM). For any given test setup, the pin will interact with the disc sample with some pressure. The contact pressure will be a function of the material properties, the geometry, and the applied load. Details regarding the contact pressure calculations will be discussed later. Regardless of the configuration, the pressure of the pin will result in a wear track to form on the disc. The wear track will be circular in shape and can be measured to obtain the wear rate of the materials. Similarly, the pin will form a wear scar. The wear scar is typically not as severe as the wear track but may also be analyzed to measure the wear rate of the materials. For a well lubricated

material interface, the goal is to have minimal to no wear on the materials. Good lubrication will prevent the materials from making severe contact and result in low friction and little to no wear [42-44].

The high temperature tribometer (HTT) used in this research is capable testing the friction performance of materials at temperatures up to 1000°C. The test materials are enclosed in a heating chamber that is wrapped in an insulating layer of gold foil. The platform that holds the disc sample, and the pin assembly fit within the heating chamber with about 1.5mm of clearance on all sides. The small clearance allows for proper heating and insulation of the test materials. This is also beneficial for room temperature tests, as it prevents drafts to enter the test area.

The entire tribometer has a metal cylinder and glass bell jar enclosure that may be lowered to maintain the environment of the testing area. The enclosure was put in place to reduce any temperature fluctuations during a given tribotest. In addition, the bell jar enclosure may be used to perform experiments under a vacuum environment. The metal cylinder and the glass bell jar have rubber gaskets at the contacting regions that create an air tight seal. A vacuum pump may then be attached to the base of the tribometer to lower the pressure inside. For this research, the samples were not tested under vacuum conditions. The entire HTT system with the bell jar enclosure lowered can be seen in Figure 5.

Figure 5. Image of the high temperature tribometer (HTT) apparatus used in this research.

The tribometer connects to an instrumentation and controls console which handles all operations and displays relevant information. The tribometer is capable out outputting an array of datasets, including friction force, friction coefficient, normal force, temperature, RPM, and position, among others. The output datasets are collected and organized using a data acquisition (DAQ) system. The data is then displayed and

saved to file using a LabView program specifically built for this research to ensure consistency and repeatability among all experiments. The program graphically displays the friction coefficient, friction force, normal force, temperature, disc position, temperature, RPM, and test time.

3.2 Point contact

The pin-on-disc tribometer setup discussed in the previous section is referred to as a zero dimensional contact, also knows a point contact. Due to the geometry of the mating materials, the area at which they come into contact is infinitesimally small; only a single point. This type of contact geometry is one of the most commonly used methods to evaluate the tibological performance of various materials [45-47].

Although this methodology is well established for dry materials, it has some issues when evaluating lubricated materials. The main issue is in regards to the flow of the lubricant and the nature of the sliding motion of the pin. Essentially, over time the lubricant will become pushed out from the wear area. At this point, the analysis becomes boundary lubrication as a best case scenario, or pure metal to metal contact at worse. When metal to meal contact occurs, the lubricant is no longer being analyzed. A true representation of the lubricant performance will be an experiment in which full fluid film lubrication in the hydrodynamic to elastohydrodynamic region is maintained [48]. Due to the small contact geometry and the highly viscous nature of grease, it is difficult to maintain a film of lubricant in the wear track area. The viscous grease will get pushed out of the track, and again due to its viscosity will not flow back into the track. However,

a pin-on-dis configuration will serve as a good basis to compare the results of newly developed tribotest methods.

A pin on disc test is a standard tribological experiment wherein a ball bearing is placed in sliding contact with a flat disc sample. The geometry in this case is referred to as point, or zero dimension (0D), due to the infinitesimally small contact region that forms for a sphere and a flat surface. Under a Hertzian contact analysis, it is assumed that the mating materials are elastic and perfectly smooth, thereby producing complete contact without gaps [49]. In addition, when two elastic bodies are placed in contact under some applied load, both elastic and plastic will occur for both materials [50]. Due to the slight deformation at the contacting point, the actual contact geometry will be circular (Figure 6). The stress distribution will vary along the circular area due to the concavity of the ball bearing. The highest stress will be located at the center of the contact area. The outside of the circle will experience lesser stresses in the form of radial stress, σ_r, and hoop stress, σ_h. A schematic diagram of the ball on disc, point contact geometry is shown in Figure 6.

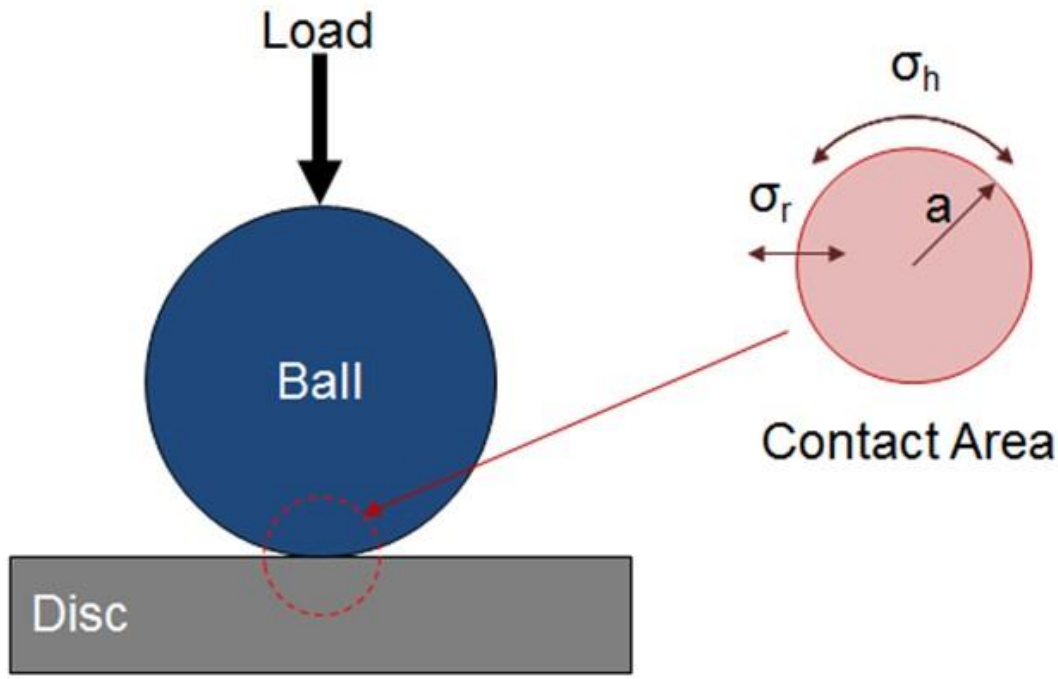

Figure 6. Schematic diagram of a ball on disc contacting surfaces with the resulting Hertzan contact geometry and stress locations.

As shown in Figure 6, the hoop stress will have an equal and opposite magnitude along the perimeter of the contact circle. Thus, the outer contact region will be simply under shear stress [51, 52]. Under static load, the maximum shear stress for this configuration will be located beneath the central point. The depth of maximum shear contact will be 48% of the total radius, r, of contact [49].

The Hertzian analysis for static contact of the ball on flat disc model was performed using a series of equations [51]. Since this analysis involves the interaction of two different materials of different geometry and mechanical properties, two relative

relations need to be established. The first is determining an effective radius for the materials. This was achieved using the following equation.

$$R^* = \frac{1}{\left[\frac{1}{R_1} + \frac{1}{R_2}\right]}$$

Equation 3.1

where R1 is the radius of the ball bearing, and R2 is the radius of the disc sample. Since the disc sample is a plane surface, the value for R2 will be zero. However, since we cannot divide by 0, the effective radius will reduce to half the ball bearing radius. The next relation that must be established is the effective elastic modulus for both materials. This was done using the following equation.

$$E^* = \frac{1}{\left[\frac{1 - \upsilon_1^2}{R_1} - \frac{1 - \upsilon_2^2}{R_2}\right]}$$

Equation 3.2

where v1 and v2 represent the respective Poisson's ratio for each material, and R1 and R2 represent the radii of the materials. Again, since the disc material is a plane surface, R2 will be equal to zero.

Now, the effective radius of the region of contact can determined using the following equation.

$$a = \sqrt{\left(\frac{3FR^*}{4E^*}\right)}$$

Equation 3.3

where *a* is the radius of the contact area (Figure 6), F is the applied load, R* is the relative radius of materials, and E* is the relative elastic modulus of the materials. The depth of contact, z, can be calculated from the radius using the following equation:

$$z = .48 * a$$

Equation 3.4

Therefore, combining all the previous information, the maximum Hertzian contact stress can be determined using the following equation.

$$P_{max} = \frac{3F}{2\pi a^2}$$

Equation 3.5

where F is the applied load, and a is the radius of the circular contact region. From the maximum contact stress, the maximum shear stress may be calculated using the following equation:

$$\tau_m = .31 * P_{max}$$

Equation 3.6

The following table lists the calculated Hertz contact values for the two materials used in the pin on disc experiment. The disc was made from 440C stainless steel, while the ball was 360L stainless steel.

Table 2. Material properties with resultant Hertian contact values.

Material 1	Material 2	R* [mm]	E* [Gpa]	r [mm]	z [mm]	σH [Gpa]	τm [Mpa]
316L	440C	1.5	351.4	0.09	0.043	3.28	1.0168

3.3 Line contact

As discussed above, using a point contact geometry has inherent issues when evaluating a lubricant such as an oil or grease. Lubricant being removed from the mating area is of concern. One method of addressing this concern is to use excess amounts of lubricant to completely cover the mating area. Once such example is the American Society of Testing and Materials (ASTM) four ball test method [53]. This test configuration uses a closed test chamber that is completely filled with lubricant. This allows for a constant flow of lubricant at the mating surfaces. Although this is a well-established method for analyzing oil, or more fluid lubricants, it does not lend well to the behavior of lubricating greases. The primary issue when analyzing grease in this method is that the viscosity of the grease will prevent it from flowing and replenishing the mating area with lubricant. Another issue is in regards to thermal effects. Lubricating greases tend to have high density, and numerous components which will affect the thermal behavior from the friction generated at the mating surfaces to the rest of the bulk [34, 54]. A new method is needed to properly evaluate the friction performance of grease.

For this research, a new testing configuration was designed to solve the issues related to grease friction testing. Based around the operation of a standard radial ball bearing configuration, a channel and ball geometry was established. The final design is shown in Figure 7.

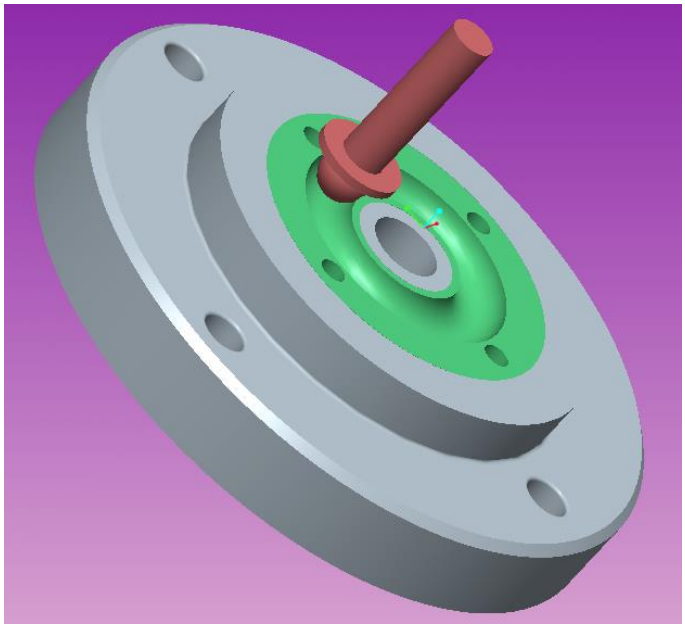

Figure 7. Diagram of the new channel and ball friction test setup for grease evaluation.

The new design is made to fit within the high temperature pin-on-disc tribometer machine. The “disc” for this setup consist of a semicircular channel that has a cup-like cross section. The “pin” is a single piece that has a collar and bearing ball welded to the end. The design of each component can be seen in Figure 8. The ball has a 0.25inch diameter, while the channel has a 0.3inch indentation diameter. Each piece is machined in such that the ball comes into contact with the bottom of the channel and has enough clearance to allow for grease to maintain a consistent layer. In this instance, the mating parts will have line, or two dimensional (2D), contact. The uniqueness of this design is in the collar at the top of the ball. When grease is introduced into the channel, and the ball set to travel around it, the collar serves as a barrier to prevent the grease from being removed. The grease that gets pushed out due to normal flow conditions will be stopped

by the collar and forced back into the channel. This allows for the mating surfaces to be continuously lubricated by the same amount of grease throughout the course of an experiment.

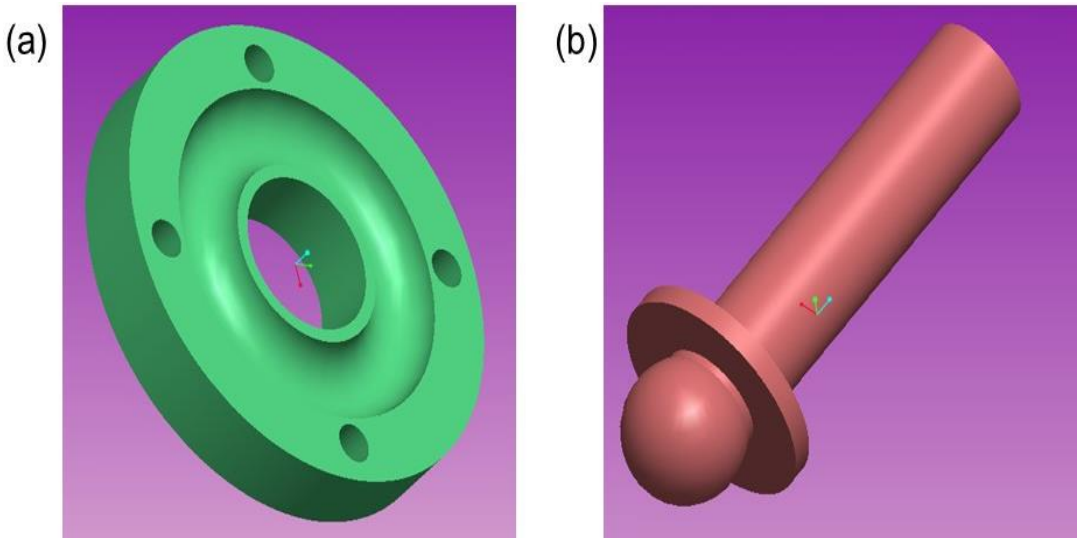

Figure 8. (a) Disc shaped insert with a 0.25inch race channel, and (b) Pin with a 0.25inch bearing ball and collar welded in place.

The new contact geometry will undergo a similar analysis to that of the pin on disc configuration discussed in the previous section. That is, a Hertzian contact analysis for line contact will be utilized [50]. Utilizing a similar methodology as discussed for the point contact configuration, the material properties and geometry of the materials were used to determine effective relationships.

The contacting geometry will not be the same as that of point contact. Instead, the contact area along the line of the mating materials will have an elliptical shape with a major and minor axis. A diagram of this geometry is shown in Figure 9. The size of the ellipse will depend on the load and the elastic properties of the materials.

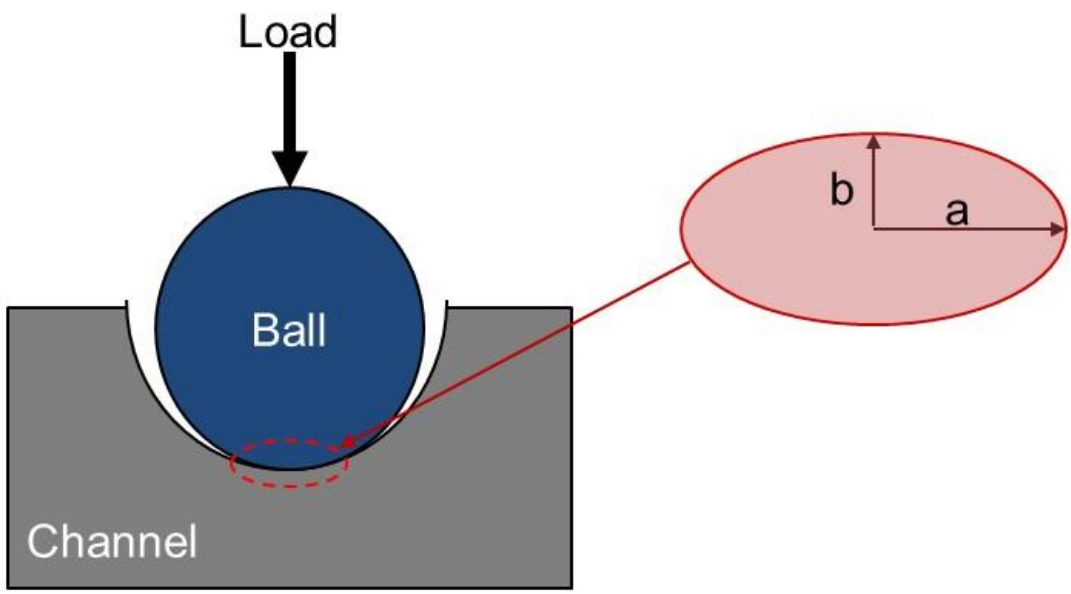

Figure 9. Schematic diagram of the two dimensional ball in channel contact.

The geometry of this configuration will have three radii that will be used to calculate the contact area and pressure. As shown in Figure 10, the ball with have a radius, R1, the channel indentation will have a radius, R2, and the channel track will have a radius R3. All of these values are constant for all of the test runs. The dimensions for the pin and channel are summarized in Table 3 below.

Table 3. Summary of the radii for the ball, channel indentation, and channel track. All dimensions in inches.

R1	R2	R3
0.125	0.15	0.75

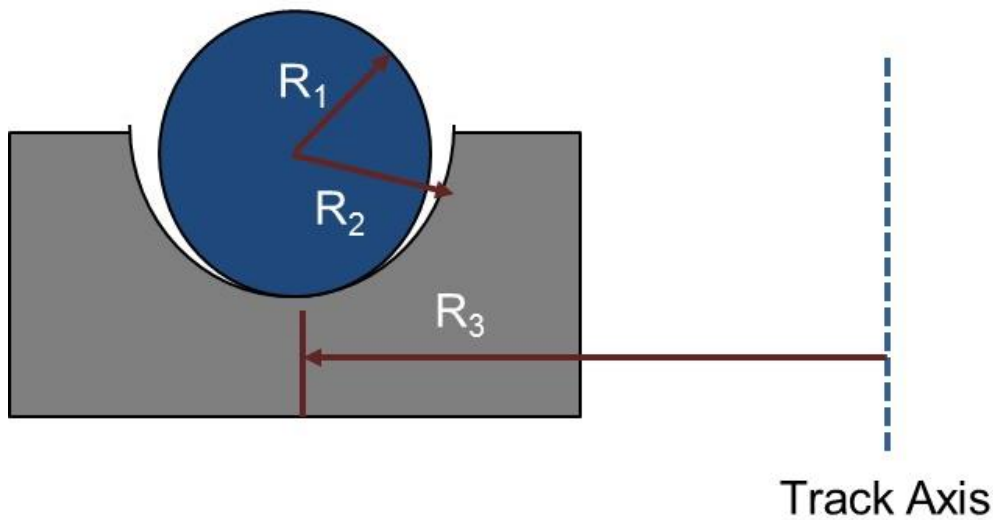

Figure 10.Schematic diagram of the geometric parameters of the contacting materials.

The values of the half widths of the major and minor axis, a and b, may be obtained through a standard analysis for the contact mechanics of a ball in cup configuration [50, 51]. This contact analysis is typically used for ball bearings inside a circular raceway, and will comply with the geometry mentioned above. The calculation of the major and minor axis values may be used to determine the Hertzian contact area. However, the approach to obtain these values requires an analysis of various geometric

and elastic properties of the contacting materials. The final equations for the major axis, a, and minor axis, b, half widths are listed below.

$$a = 1.145 n_a \sqrt[3]{FK\gamma}$$

Equation 3.7

$$b = 1.145 n_b \sqrt[3]{FK_2\gamma}$$

Equation 3.8

where F is the applied load, K is a geometric constant relating the radii of all components, and γ is a constant relating the elastic properties of each material. The values for n_a and n_b are found through integrating across the ellipse. The value for K may be found using the following equation:

$$K = \frac{1}{\frac{2}{R_1} - \frac{1}{R_2} + \frac{1}{R_3}}$$

Equation 3.9

where R_1 is the radius of the ball, R_2 is the radius of the channel indent, and R_3 is the radius of the channel race. The values for the radii are listed in Table 3 above. The value for γ in the equations for a and b may be found using the following property relation:

$$\gamma = \frac{(1 - v_1^2)}{E_1} + \frac{(1 - v_2^2)}{E_2}$$

Equation 3.10

where v_1 and v_2 are the Poisson's ratio for the ball and channel, respectively and E_1 and E_2 are the elastic modulus for the ball and channel, respectively.

The maximum Hertzian contact pressure between the mating parts will act along the center of the contacting region. The maximum contact pressure can be calculated using the following equation:

$$p_{max} = \frac{2F}{\pi b L}$$

Equation 3.11

where F is the applied load, b is the half width found with Equation (1), and L is the contact line length. The mean pressure along the contact region can be calculated with the following equation:

$$p_{mean} = \frac{\pi p_{max}}{4}$$

Equation 3.12

The pin is made from 360 stainless steel, while the disc is made from 440C stainless steel. The ball bearing and channel each have a diameter of 6mm. Taking the

material properties into account, the Hertzian contact stresses can be calculated. The results of the calculation are listed in the following table.

Table 4. Results of a Hertxian contact analysis of the two mating materials.

Material 1	Material 2	b [mm]	Pmax [Mpa]	Pmean [Mpa]
360	440C	0.036	185.4	145.54

3.4 Environmental conditions

Many lubricating grease are meant to perform under extreme environmental conditions. The thread compound greases used in the oil and gas industry for example must be able to operate at up to 350°C temperatures and 200Mpa pressures for deep well drilling [55-57]. For reasons such as this, it is necessary to evaluate lubricants at various temperatures. In this study, the lubricating greased will not only be evaluated at room temperature but at cold and high temperatures as well. The aforementioned high temperature pin on disc tribometer (HTT) is capable of operating at up to 1000°C. For this study, greases will be evaluated at 100 and 200oC. In order to test at low temperatures, the HTT required slight modification. Liquid nitrogen will be introduced to the system to reduce the temperature below freezing. Therefore the entire system was insulated and sealed to ensure a consistent ambient temperature within the test chamber. Liquid nitrogen was let into the system such that the temperature reached a steady -50oC

and -100oC. An image of the modified HTT with liquid nitrogen tank is shown in Figure 11. The choice of high and low temperature values was completely arbitrary and were simply chosen to evaluate a wide range of operating temperatures for the lubricating greases.

Figure 11. High temperature tribometer (HTT) modified to accept liquid nitrogen for low temperature experiments.

3.5 Results of tribotesting

Tribotesting was conducted on four groups of grease samples. One was a commercially available compound called NCS-30. This compound is an industry standard that contains several non-metallic particle additives. The second group consisted of a mixture of NCS-30 and 2.3wt% Fe3O4 particles. The third groups consisted of a clean base lubricant in the form of petroleum jelly. Finally, the fourth group consisted of a mixture of petroleum jelly and 2.3wt% α-ZrP nanoparticles. A list of all the groups can be seen in Table 5. The mixing process for Groups 2 and 4 were very simply achieved. A glass stirring rod was used to mix the particles by hand until an even coloration was achieved.

Table 5. List of all grease sample test groups.

Group 1	Group 2	Group 3	Group 4
NCS-30 (Reference Compound)	NCS-30 + 2.3%wt Fe_3O_4	Petroleum Jelly	Petroleum Jelly +2.3wt% ZrP

All four grease groups underwent tribotesing using the point and line contact geometries in the HTT. Experiments were performed at room temperature (25ºC), high temperature (100ºC and 200ºC), and low temperature (-50ºC and -100ºC) to evaluate the integrity of the grease at various environments. The test parameters for all samples was the same throughout. The tribometer was set to rotate at 25RPM. One complete rotation

constituted a complete cycle. A total of 250 cycles were evaluated for each grease (10 minute test time total). The loading of the pin was set to 3lbs. Temperatures were adjusted accordingly. Each group was evaluated based on average friction coefficient for each parameter. The results of the point and line contact experiments are listed in Table 6 and Table 7, respectively.

Table 6.Average coefficients of friction of each grease group for point contact at various temperatures.

Group	T_1	T_2	T_3	T_4	T_5
	-100	-50	25	100	200
1	0.251	0.235	0.201	0.221	0.245
2	0.293	0.275	0.245	0.261	0.301
3	0.341	0.284	0.223	0.201	0.188
4	0.301	0.254	0.185	0.181	0.177

Table 7. Average coefficients of friction of each grease group for line contact at various temperatures.

Group	T_1	T_2	T_3	T_4	T_5
	-100	-50	25	100	200
1	0.195	0.164	0.12	0.157	0.174
2	0.25	0.193	0.17	0.183	0.22
3	0.223	0.204	0.188	0.163	0.122
4	0.184	0.143	0.131	0.101	0.091

The results showed that friction coefficient tented to be higher for the point contact geometry in all cases. This can be attributed to the grease becoming removed from the wear area, causing metal to metal contact to occur. In contrast, lower friction

was observed for the line contact geometry. A graphical representation of the friction results for point and line contact at all temperatures can be seen in Figure 12 and Figure 13, respectively.

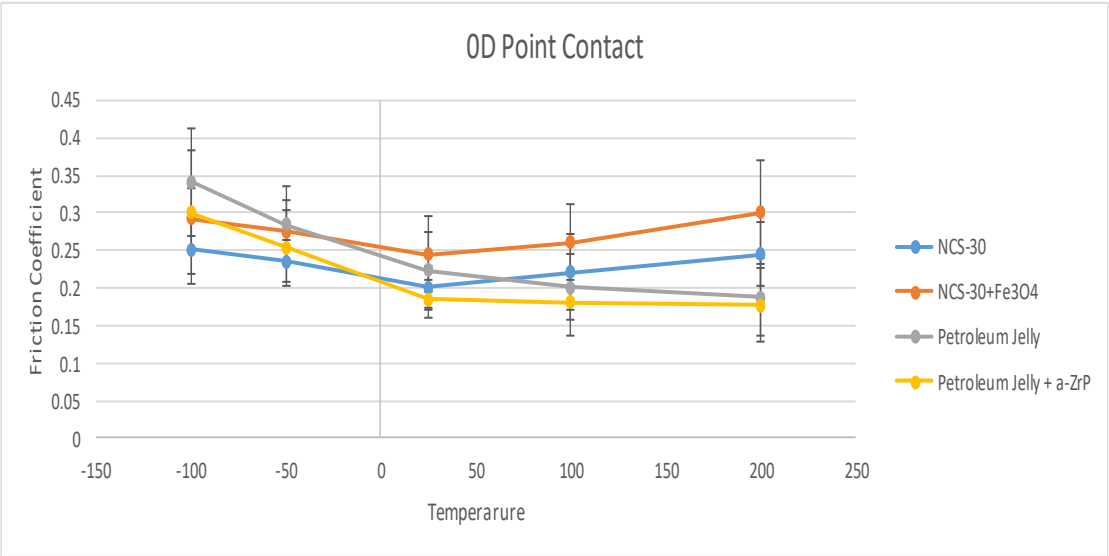

Figure 12. Plot of friction coefficient versus temperature for all four grease groups under sliding point contact geometry.

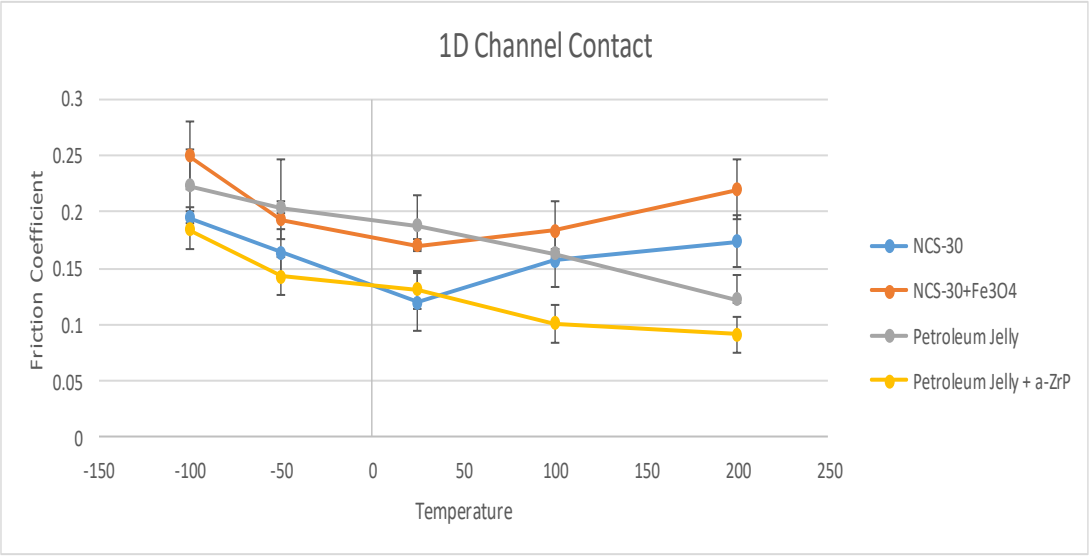

Figure 13. Plot of friction coefficient versus temperature for all four grease groups under sliding point contact geometry.

It is also important to note that temperature had a varied effect of all grease groups. At high temperatures, Groups 1 and 2 tented to become thicker and less fluid. This may be attributed to the oxidation of some of the grease components within the compound. At high temperatures, the friction coefficient of Groups 1 and 2 increased compared to room temperature. In contrast, Groups 2 and 3 appeared to perform better at elevated temperatures. The petroleum jelly become more fluid at elevated temperatures. This allowed the lubricant to flow more effectively between the mating surfaces, maintaining a lubricating film, and reducing friction throughout. Low temperatures tended to have similar effects across all grease groups. In all cases the grease mixtures became harder and less fluid. This tendency greatly restricted its movement, thereby

causing higher friction to occur. In regard to the effect of particle additives. It was clearly shown that the iron oxide particles had a negative effect on the NCS-30 base lubricant, while the zirconium phosphate particles improved friction performance. This relationship will be expanded in a later chapter.

CHAPTER IV

TWO DIMENSIONAL CONTACT

This chapter provides information regarding the methodology used to analyze area contact of two dimensional surfaces, including the design and implementation of new configurations.

4.1 Design strategy and configuration for grease evaluation

To better understand the flow and interactions of grease between sliding surfaces, a new design was made to build a new configuration. This testing machine was developed during the early stages of this research and has since been established as providing reliable results for grease compounds used in the oil and gas industry.
In conjunction with an American Petroleum Institute (API) Workgroup, the machine was established to quantify frictional performance of thread compounds. Thread compounds are a specific type of grease lubricant that contain numerous types of additives in varying quantities. The nature of these compounds was discussed in an earlier section. The machine is meant to simulate the working conditions of rotary shouldered connections that are commonly used for deep well drilling. Details of the original test used to evaluate these compounds are outlined in API Recommended Practice 7A1 and will discussed in further detail below [58].

To investigate thread compounds for frictional performance and galling resistance, it is best to test them under real world conditions. These grease mixtures are meant to lubricate, protect, and seal the threaded connections of standard oil well drill

pipe; commonly referred to as tubing and casing connections.. A typical tubing and casing connection consists of a threaded “pin” and a corresponding threaded “box,” as shown in Figure 14.

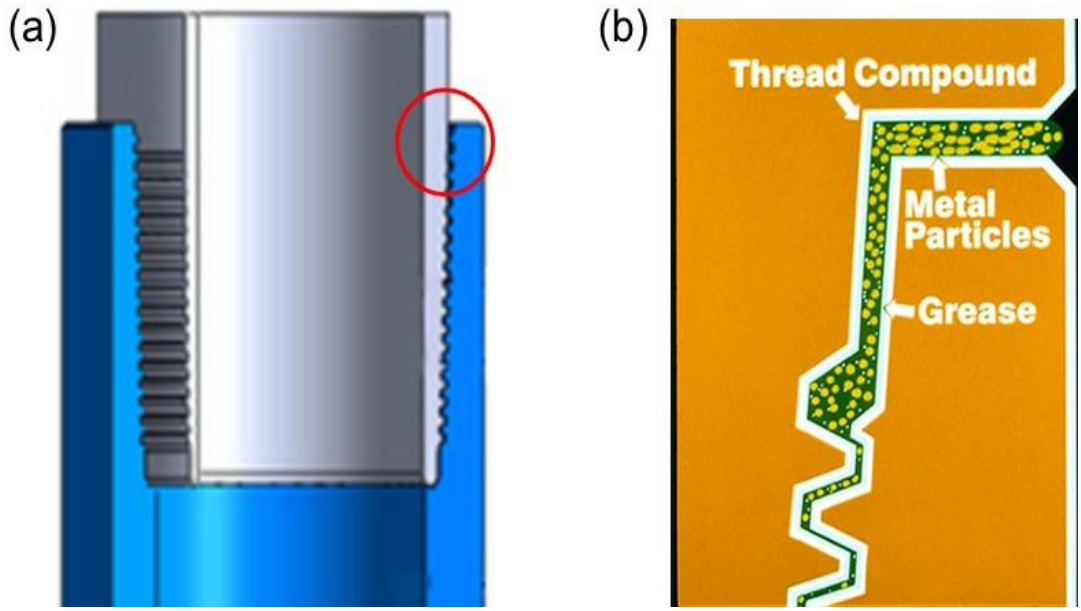

Figure 14. (a) Cross sectional view of a typical threaded connection for tubing and casing joints; and (b) Close up view of the mating threads coated in thread compound.

The thread compounds must also prevent galling of the mating surfaces. Galling is characterized by a severe form of plastic wear as a result of cold welding of the mating surfaces. Examples of galled surfaces can be seen in Figure 15. Many factors may contribute to galling such as material composition, high friction, high pressure, and

temperature [59-62]. Materials of the same type will have a greater tendency to cold weld together due to the tendency of the outer surfaces to chemically react with one another. A typical practice in API is to use mismatched material pairs (one Inconel A17 and one P550 for example) for drill pipe to avoid this scenario. Standardized testing methods that evaluate galling resistance of materials are ASTM G98 and G196 [63]. As stipulated by these standardized testing methods, well lubricated surfaces will not experience galling. However, given the working conditions of API thread compounds, galling is of serious concern and a method to properly evaluate lubricants is needed.

Figure 15. Examples of galling damage on tubing threads and on a flat disc shaped metal specimen.

The standard testing method developed by API, utilizes a 1 inch diameter bolt and corresponding nut to simulate a typical rotary shouldered connection (RSC). The nut and bolt are first coated in the thread compound of interest, then the pair are loaded into a machine that rotates them together until a certain torque level in reached. A clockwise rotation is known as the "Make-Up," while a counter clockwise rotation is referred to as a "Break-Out." For any given evaluation, the grease, nut, and bolt system are Made-up to a specified torque. They are then Broken out to separate them. For both instances, the machine will measure the torque value versus the rotation. A diagram of the API 7A1 setup is shown in Figure 16a.

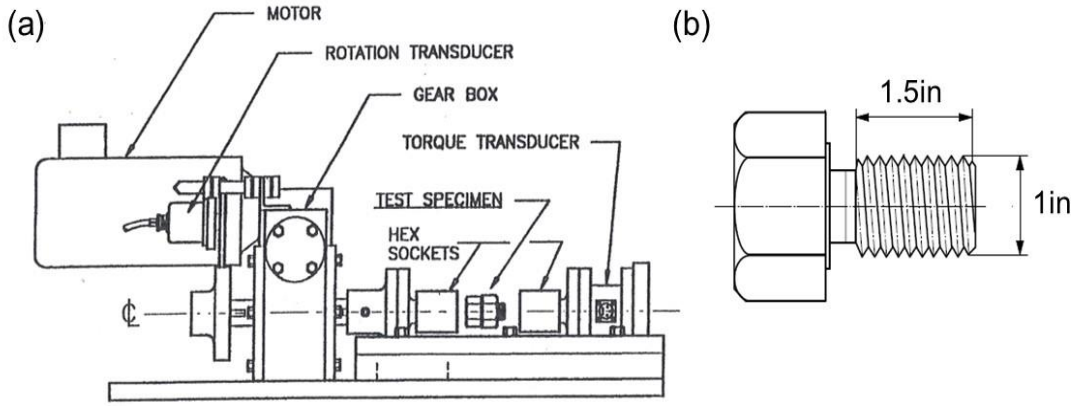

Figure 16. (a) Diagram of the major components of the standard API 7A1 machine used for evaluating thread compounds; and (b) Drawing of a standard 1 inch bolt used for the tests.

The proposed research has built upon the equipment and procedure that was established under API 7A1. The major contribution is the integration of a load cell in line with the hardware, as well as a software upgrade to handle the data acquisition. The load cell sits inside a large cylindrical assembly that has a one inch diameter threaded rod running through the center, as seen in Figure 17. The load cell sits at the bottom of the cylinder, while steel disc spacers sit on top of it and extend toward the top of the cylinder. The top most spacer extends about half an inch above the top of the cylinder. An end cap is then placed on top of that spacer and loosely secured to the wall of the cylinder with four bolts. The purpose of the end cap is to transmit the force being applied to the test specimens to the spacers, then to the load cell to be recorded. Two load cell assemblies were built, one that has a 100,000 pound (444822N) limit, and another that has a 200,000 pound (889644N) limit. Each assembly has the same configuration, only the dimensions differ according to the diameter of the load cell. The one inch diameter threaded rod remains the same regardless of the load cell.

The test specimens will be mated together and placed over the threaded rod at the top of the load cell assembly as shown in Figure 17. The specimen in contact with the end plate has three pins that will prevent it from rotating during a test. The second specimen is attached to a one inch nut with a similar pin configuration. As the nut is rotated by the machine on one end, the test specimens will get rotated against each other, causing the load cell to become engaged. The load cell data is then collected by LabView software, and can be used to evaluate the frictional performance of the lubricating grease under investigation.

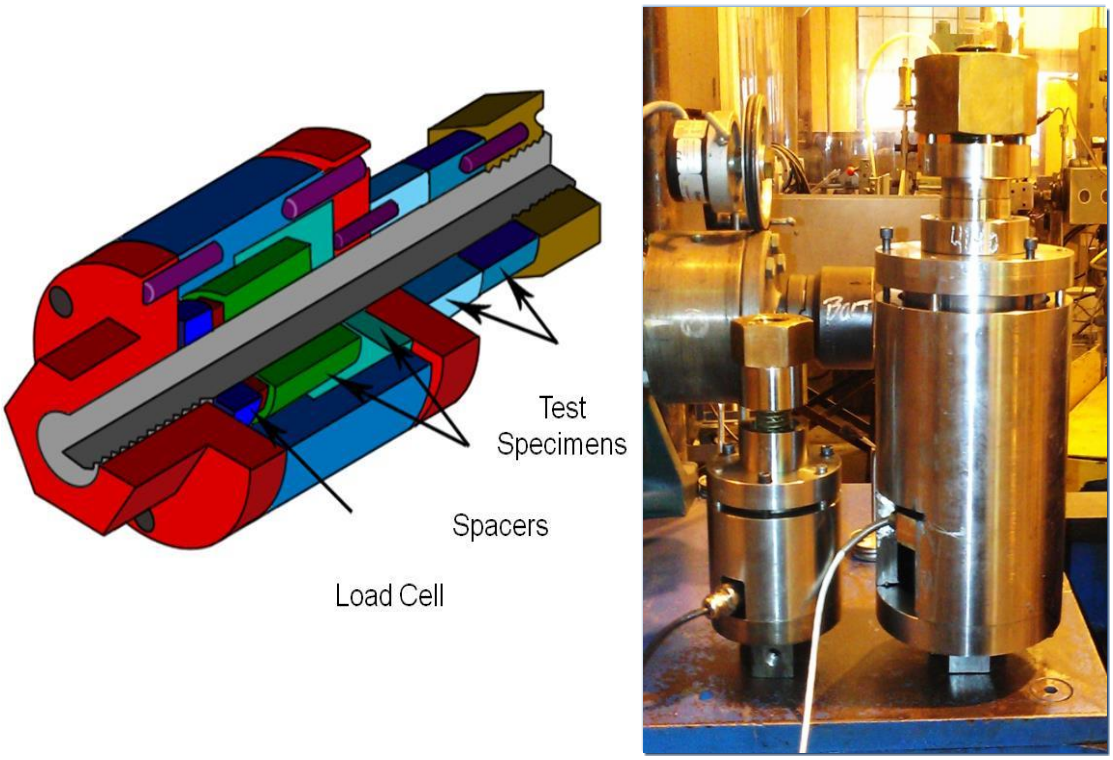

Figure 17**.** New load cell assembly that was integrated into the original API 7A1 machine.

The original 1 inch bolt test specimen (Figure 16b) was replaced with a pair of ring shaped test specimens in order to establish a proper surface area measurement. The new specimens fit in-line with the load cell assembly, as seen in Figure 17, and can be seen in greater detail in Figure 18. As shown in the figure, both specimens are held on either side of the assembly using pins. One specimen remains stationary, while the other is allowed to rotate against it. This configuration allows for simultaneous measurement

of the torque produced, as well as the resultant load being applied. A complete configuration of the new machine setup can be seen in Figure 20.

The new tests specimens (Figure 18A) have an inner and outer diameter of 1.5in, and 1.9in respectively. The total surface area is 1.07in^2. The samples are machined from various materials including: 4140 Steel, Inconel A-718, P550 Steel alloy, and P530 Steel alloy. The material selection was in accordance with materials that are typically used for rotary shoulder connections (RSCs) in the oil and gas industry [64, 65].

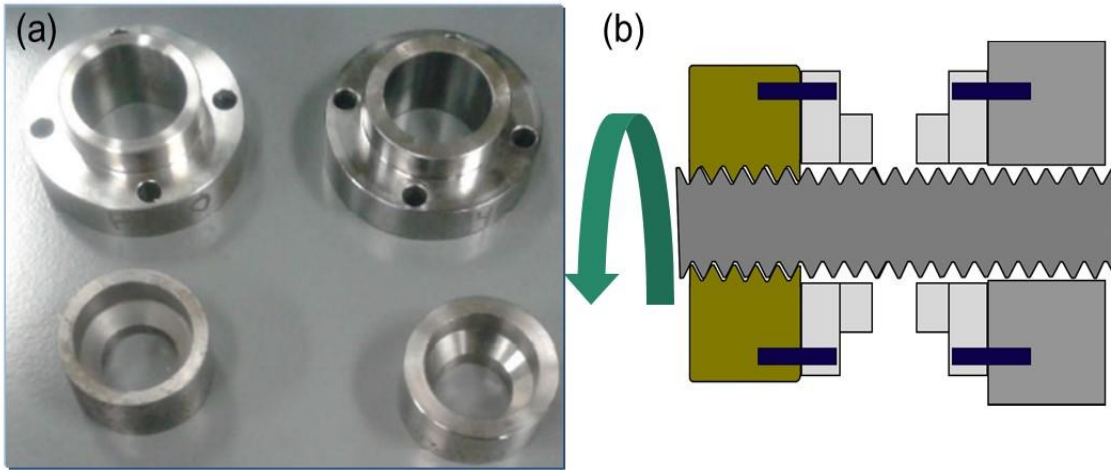

Figure 18. (a) Image of the new ring shaped test specimens; and (b) Diagram of how the specimens fit into the new load cell assembly, illustrating the dynamic (left) and stationary (right) specimens.

When evaluating a lubricating grease sample, the tests specimens are first thoroughly cleaned and polished to a roughness of at least 3.2+-0.4um Ra. This is to ensure that no surface defects will interfere with the test condition. After cleaning the specimens, an even coating of grease is applied to both faces as shown in Figure 19a. The specimens are then loaded into the machine for testing (Figure 19b). The dynamic specimen will rotate along the threaded rod toward the static specimen. As this occurs, a torque and a load will simultaneously be applied and measured. The collected data will then be used to evaluate the grease performance. After a single test "run," the specimens are removed and thoroughly cleaned once again. After cleaning, new grease is added and the test is repeated. In order to gain a good statistical representation of the grease performance, a total of twenty four test runs will be conducted. Eight test runs will be performed on a standardized grease compound of known performance, then eight on the grease under investigation, and finally eight more on the standardized compound. The statistical analysis will be discusses in a later section.

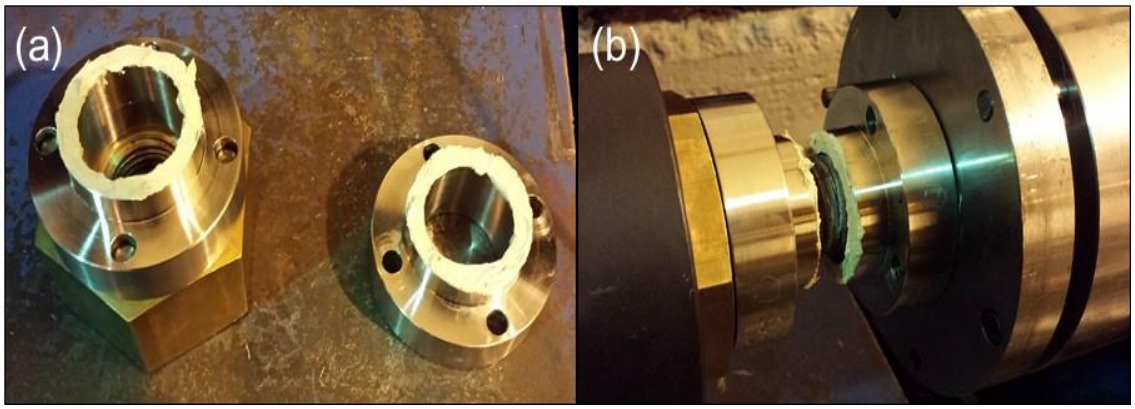

Figure 19**.** (a) A tests specimen pair with an even coating of grease applied; and (b) The coated tests specimens loaded into the machine for testing.

In addition, this new configuration allows for the collection of the used grease after each test. The used grease will undergo the same evaluation that was conducted on the as received, “clean” grease. Comparative data may then be used to gain a deeper understanding of grease degradation over various test conditions.

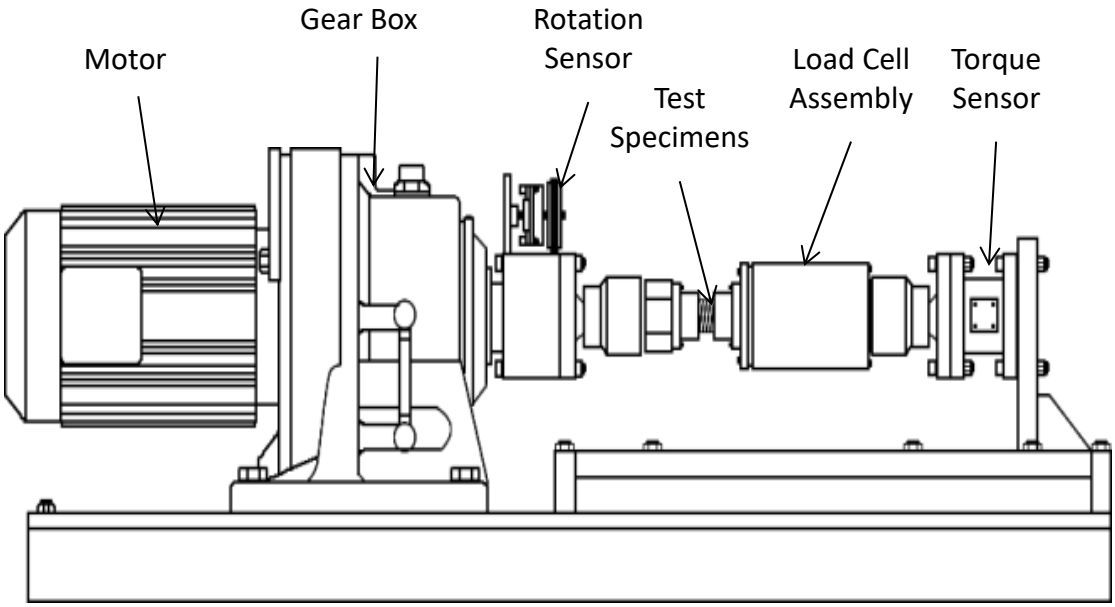

Figure 20. Diagram of the new configuration meant to evaluate the frictional performance of grease.

4.2 Calculations and data analysis

The new test configuration has a complex area contact region that involves both the ring shaped specimen contact, and the thread contact between the nut and threaded rod that force them together. This configuration represents a complex two dimensional contact. A diagram of the contacting regions are outlined in Figure 21.

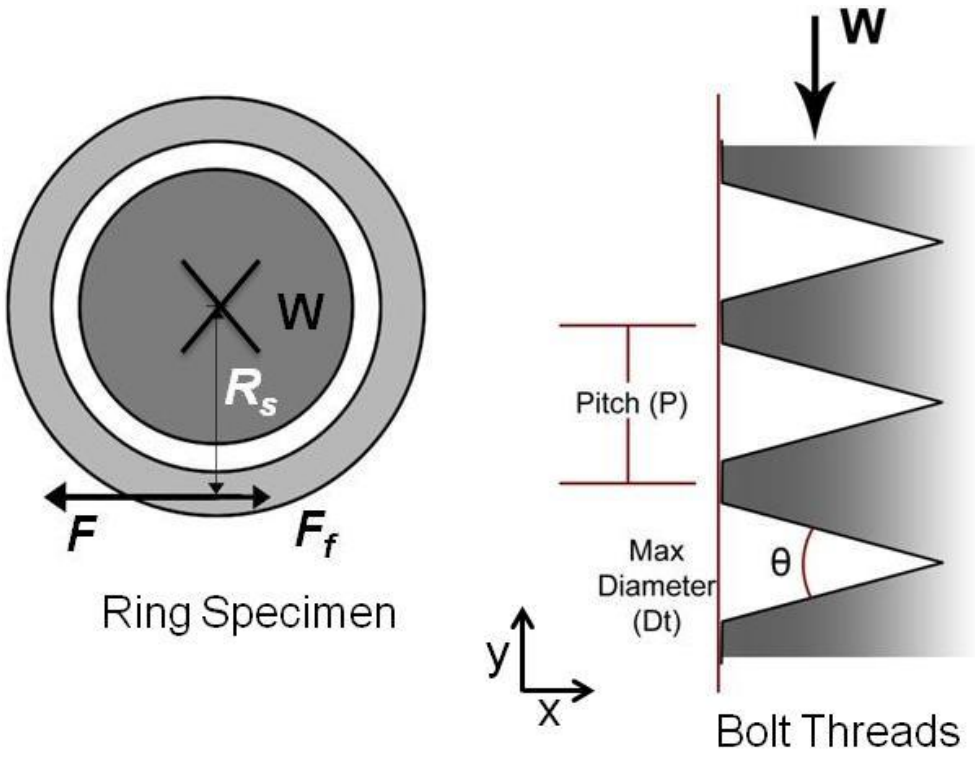

Figure 21**.** Diagram of the forces acting on the ring specimen and the bolt threads, as well as important dimensions under consideration.

As shown in Figure 21, the primary forces acting on the test specimen and the threads will be the load, W, the tangential force, F, and the resultant frictional force, F_t. As the diagram shows, the load, W, acts into the page when acting on the ring sample, while acting perpendicular to the bolt threads. Considering the diagram in Figure 21, the geometric relationships can be used to determine the friction coefficient of the tribo-system as:

$$\frac{F}{W} = \frac{\frac{f}{\cos\theta} + \tan\lambda}{1 - f\frac{\cos\theta}{\tan\lambda}} + f\frac{R_s}{R_t}, \text{ with } \lambda = \frac{P}{\pi D_t}$$

Equation 4.1

where F represents the tangential force, W represents the load acting on all surfaces, f is the friction coefficient, θ is the thread angle, R_s is the average radius of the ring specimen, R_t is the radius of the bolt threads, P is the thread pitch, and D_t is the thread diameter. By re-arranging these terms and simplifying, the friction coefficient can be determined with the following equation:

$$f = \frac{\left(\frac{T}{W} - \frac{P}{2\pi}\right)}{\left(\frac{D_t/2}{\cos\theta} + R_s\right)}$$

Equation 4.2

where T represents the torque that is directly measured from the machine. By using this relationship, the friction coefficient may be quantified for any grease compound tested on this machine. In addition, the machine can also produce a “Friction Factor,” value as outlined in API 7A1 [58]. When comparing the performance of one grease to that of a standard reference grease, the friction factor is determined based on the average slope of the “Make-Up” torque curve over multiple tests. The “Make-Up” torque is an industry

term that refers to the amount of rotational torque required to “make up,” or put together, a tubing a casing connection joint. For this purpose, a series of 24 total tests must be conducted in order to obtain reliable and repeatable results. A reference grease of known performance is first tested 8 times up to a specified torque value, followed by 8 tests for the grease of interest, and then finished with the reference grease for a final 8 tests. The slopes of each of the Make-Up torque curves between the values of 200 ft-lbs and 300 ft-lbs are then calculated. The average slopes of each data set are then inserted into the following equation to obtain the friction factor:

$$FF = \frac{2 * S_{TC}}{S_{ref\,1} + S_{ref\,2}}$$

Equation 4.3

where S_{TC} represents the average slope of the Make-Up torque slope of the grease being investigated, and S_{ref1} and S_{ref2} represent the first and second set of average slopes of the Make-up torque curve for the reference grease, respectively. The machine can obtain this result using the original 1 inch bolt configuration (Figure 16), as well as the new configuration with the load cell (Figure 18-Figure 20). Since the friction factor represents a ratio of performance of a well-established compound versus that of a newly developed compound, the closer the value computes to 1.0 the better it is considered to perform. This information can be combined with the friction coefficient measurement to obtain a more accurate and reliable representation of the grease performance.

The aforementioned reference grease is a 60% lead based compound that was an industry standard for many years. Lead is a very soft, yet durable metal that deforms easily under applied pressure. The lead additive powder would create a protective film on the surface of the threads that both reduced friction and produced a leak tight seal. However, new regulations in the oil and gas industry recommend using a calcium fluoride (CaF) based compound, as it is non-toxic [58]. Lead based compounds in general have all been phased out over the years due to government regulation over health and environmental concerns [66]. However, small batches of lead based compound will be used as a basis for evaluating new compounds moving forward. Special handling and attention will be paid with these compounds to assure the safety of the operator.

The machine developed for this research can directly output torque versus rotation, and load versus rotation. A sample data plot is shown in Figure 22.

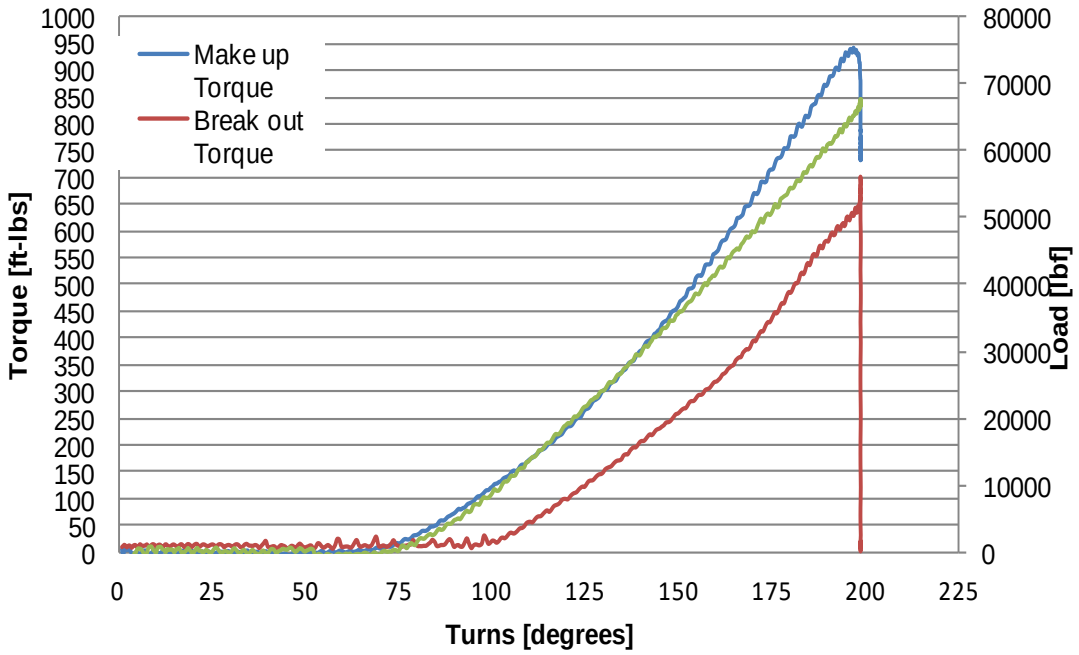

Figure 22. Typical Make-Up and Break-Out torque, and load versus rotation plot of a standard grease compound.

The machine has proven to output consistent data for any type of grease compound, regardless of the formulation. Based on the collected data, the friction coefficient may also be calculated at various torque and load values throughout the test. The friction coefficient may only be calculated when the new testing configuration is employed; it cannot be calculated from the torque data alone. Figure 23 shows an example coefficient of friction plot that was calculated over the tested load range.

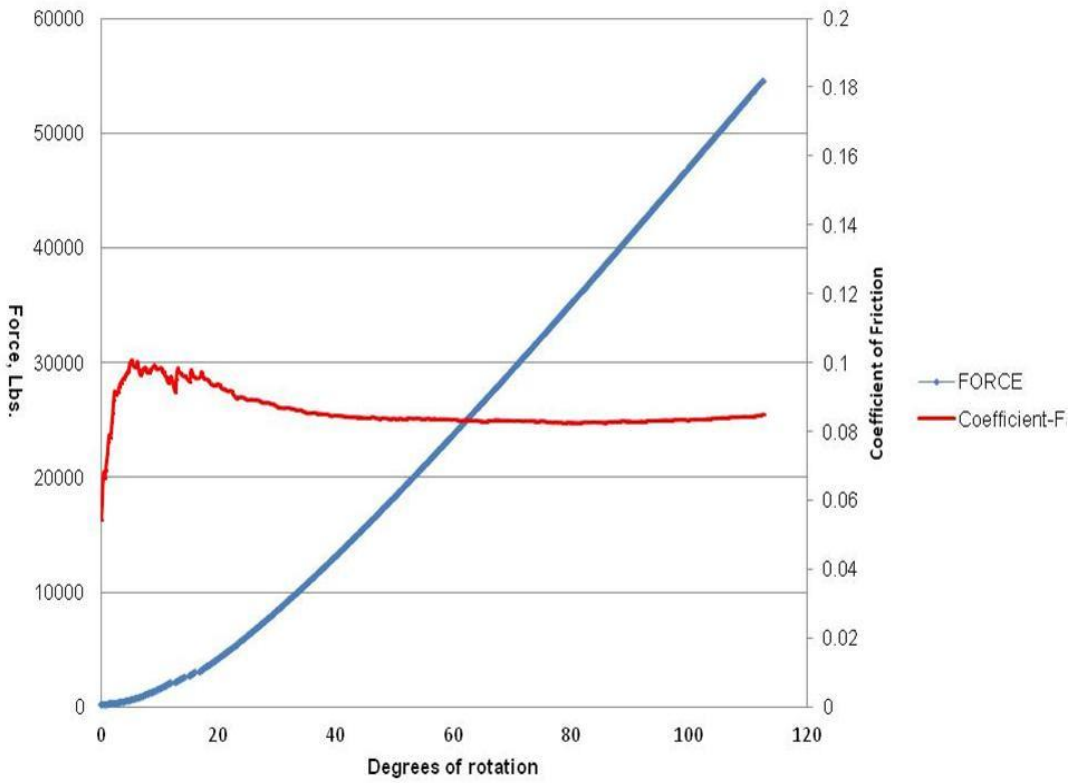

Figure 23. Plot of the calculated friction coefficient versus the rotation.

As the plot shows, the friction has a high peak at low loads, but tends to decrease and even out as the load is increased. This behavior can be observed for various grease compositions and used to better evaluate overall performance. By applying this same methodology, a grease with varying composition of additives may be evaluated in terms of friction coefficient over the same tested load range.

4.3 Grease additive evaluation

The incorporation of additives in grease formulation can have significant impact on its performance. Figure 24 shows a grease that had varying concentrations of a particular additive, and tested under the same conditions.

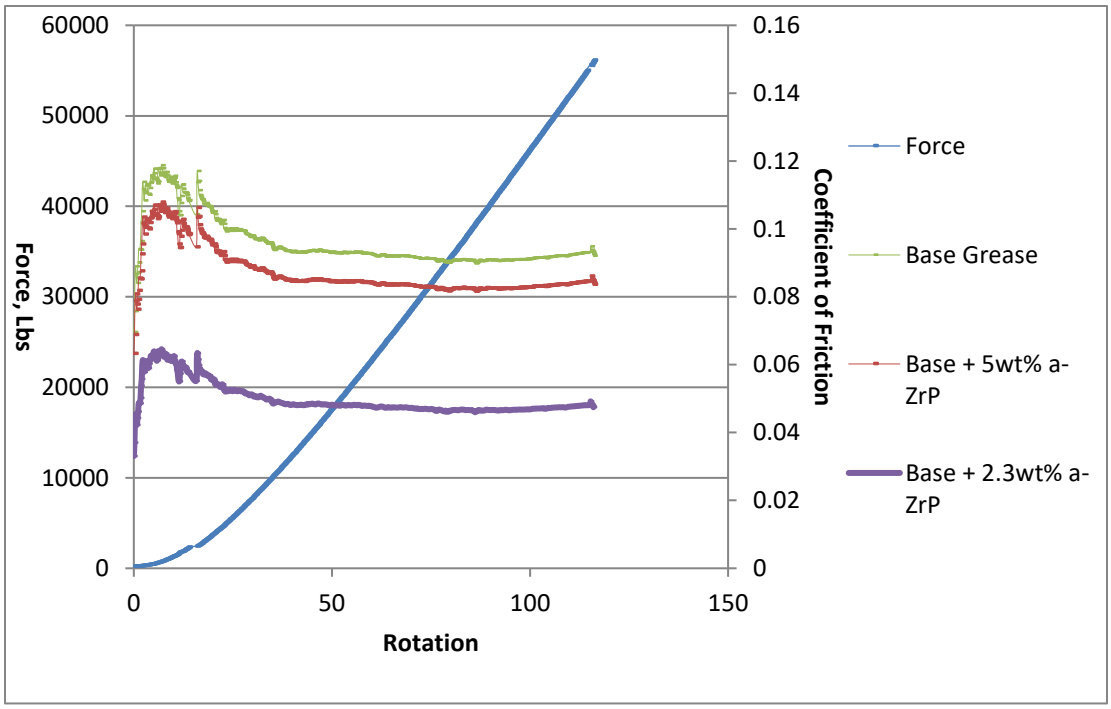

Figure 24. Plot of friction coefficient versus rotation for a grease of varied additive composition.

As the plot shows, the higher concentration of additive resulted in significantly reduced friction coefficient. However, by adding a small amount the friction coefficient increased

slightly from the original base grease. This result lends to the validity of the machine as it has been frequently shown that additive incorporation does not always lend to better performance [36, 67-69]. Likewise, the concentration of additives does not provide a definitive relationship to performance. The concentration of any particulate additive will need to be investigated to ensure optimum performance.

Inorganic particle additives in grease lubricants have played important roles in reducing frictional losses and preventing wear of mechanical systems [70-72]. For this research investigation, two common nano-sized additives will be evaluated; iron oxide, and zirconium phosphate. The base grease formulation to be used will be NCS-30 and petroleum jelly. NCS-30 is a common thread compound used to makeup tubing and casing connections and was provided by Jet-lube (Houston, TX). Petroleum jelly is a lubricant made through the refining of pure petroleum oil and was purchased at a local pharmacy.

Iron oxide, also known as rust, is a common particulate found in tribosystems as a result of oxidation, tribo-chemical reactions, and the wearing of steel materials [73-75]. The formation of iron oxide within a lubricant has detrimental effects to the mating materials due to its hardness. Third body wear is prevalent in a system that has sufficient amounts of hard oxide particles, resulting in an increased coefficient of friction during the service life. Applying this information, incorporating iron oxide nanoparticles into a lubricating grease should increase the friction coefficient and overall reduce its performance.

To investigate the effects of iron oxide nanoparticle additives in grease, a small amount was mixed into NCS-30 thread compound. Iron (II, III) oxide (Fe3O4, 99.99%) was obtained from Sigma-Aldrich and was used as received without any further processing or purification. The shape of the particles was spherical, and the average size was 100nm+-50nm. The base grease was mixed with 2.3wt% of Fe3O4 particle additives. The mixing process was carried out by stirring the grease by hand for several minutes until a uniform coloring was achieved. The original color of the base grease is a light cream, while mixing with the iron oxide turns it a grey tint. It is difficult to ensure complete homogeneity, but the uniform coloration was a good indicator that the additive was thoroughly mixed. Similarly, the effects of a-ZrP nanoparticles were investigated by mixing a small amount into pure petroleum jelly. As a control, pure petroleum jelly without additives was tested and labeled as Group 3. Similar to the iron oxide, 2.3wt% of a-ZrP nanoparticles was mixed into the petroleum jelly. The grease compound was mixed for several minutes until a uniform coloration was achieved. Four groups of grease were evaluated for frictional performance, a control grease of plain NCS-30, NCS-30 with 2.3wt% iron oxide particles mixed in, pure petroleum jelly, and petroleum jelly mixed with 2.3wt% a-ZrP nanoparticles. The test groups are summarized in Table 8.

Table 8. List of grease sample test groups.

Group 1	Group 2	Group 3	Group 4
NCS-30 (Reference Compound)	NCS-30 + 2.3%wt Fe_3O_4	Petroleum Jelly	Petroleum Jelly +2.3wt% ZrP

The two grease compound groups were tested against the industry standard 60% lead compound. A total of 24 test runs were conducted to evaluate each group using the friction testing machine discussed above. The metal tests specimens used were 440C stainless steel, a common alloy used in the oil and gas industry. This material is commonly used for bearing applications as well. The metal test specimens were prepared according to the testing procedure and inspected after each test run for any surface defects resulting from the rubbing of the grease at high contact pressure. In all cases, the metal test specimens did not experience significant wear and only showed slight changes in surface roughness. The details of the surface analysis will be discussed in a later section. The test results for Groups 1-4 can be seen in Table 9-Table 13, respectively.

Table 9. Summary of the data collected for a complete torque test of Group 1, NCS-30 reference compound.

Run No.	Thread Compound	M/U Torque (ft-lbs)	B/O Torque (ft-lbs)	B/O to M/U Ratio	Upper Torque Curve Fit (ft-lbs)	Lower Torque Curve Fit (ft-lbs)	Points Curve Fit	Slope of Line (ft-lbs/deg)	Mean Square Error	Max Load [lbs]
1	Ref_Pb	483.3	333.5	69.00	302.1	203.8	172	3.52	1.36	61716
2	Ref_Pb	475.8	316.0	66.40	304.7	200.9	186	3.55	1.92	61765
3	Ref_Pb	471.2	314.9	66.83	302.5	203.6	186	3.56	1.89	61683
4	Ref_Pb	470.9	307.3	65.26	307.4	201.1	192	3.44	1.39	62139
5	Ref_Pb	459.5	298.2	64.88	301.0	200.4	174	3.63	2.10	62090
6	Ref_Pb	465.5	302.9	65.07	301.0	200.2	182	3.64	1.45	62204
7	Ref_Pb	462.6	310.3	67.09	306.3	201.5	178	3.68	1.74	62269
8	Ref_Pb	459.3	293.4	63.89	302.7	201.3	186	3.46	1.84	61960
9	NCS30	451.5	262.1	58.06	307.7	201.6	229	3.46	1.88	62232
10	NCS30	459.6	274.0	59.61	302.6	202.2	214	3.65	1.91	62899
11	NCS30	438.9	257.6	58.68	301.4	201.4	215	3.63	2.02	62492
12	NCS30	435.7	259.9	59.65	301.3	200.7	220	3.26	2.06	62833
13	NCS30	434.3	251.5	57.92	301.5	201.9	214	3.33	1.45	62817
14	NCS30	441.8	264.2	59.79	301.3	200.2	201	3.45	2.08	62980
15	NCS30	425.5	249.2	58.57	300.8	201.9	215	3.52	2.10	62606
16	NCS30	438.2	261.5	59.68	302.1	200.0	216	3.61	1.97	62508
17	Ref_Pb	466.1	300.0	64.36	306.3	200.4	207	3.25	2.54	62022
18	Ref_Pb	460.6	293.8	63.79	300.0	200.1	193	3.40	2.18	62591
19	Ref_Pb	446.0	285.5	64.01	305.3	202.1	187	3.47	2.65	62494
20	Ref_Pb	447.6	285.9	63.87	300.3	200.6	191	3.36	1.29	62526
21	Ref_Pb	443.2	279.9	63.15	305.2	202.2	187	3.50	1.98	62396
22	Ref_Pb	448.2	288.2	64.29	302.0	201.0	177	3.56	2.12	62672
23	Ref_Pb	446.3	293.3	65.72	300.4	200.5	182	3.47	1.40	62169
24	Ref_Pb	449.2	287.2	63.94	304.6	200.4	186	3.58	1.88	62217

Table 10. Summary of the data collected for a complete torque test of Group 2, NCS-30 + 2.3wt% Fe3O4.

Run No.	Thread Compound	M/U Torque (ft-lbs)	B/O Torque (ft-lbs)	B/O to M/U Ratio	Upper Torque Curve Fit (ft-lbs)	Lower Torque Curve Fit (ft-lbs)	Points Curve Fit	Slope of Line (ft-lbs/deg)	Mean Square Error	Max Load [lbs]	Max Angle [degrees]
1	Ref_Pb	354.3	225.4	63.60	300.6	200.7	103	6.35	1.56	48352	208
2	Ref_Pb	347.4	221.1	63.65	300.8	200.4	127	4.99	1.70	50159	206
3	Ref_Pb	353.4	218.9	61.95	301.3	200.7	118	5.62	2.54	49280	232
4	Ref_Pb	347.8	219.8	63.21	301.2	200.7	129	4.97	1.74	51265	190
5	Ref_Pb	356.0	221.0	62.10	300.6	201.2	129	4.94	1.69	52047	244
6	Ref_Pb	351.7	218.2	62.04	300.9	201.2	132	5.15	1.96	52014	187
7	Ref_Pb	352.8	217.0	61.50	300.8	201.4	134	4.77	1.57	52958	309
8	Ref_Pb	344.5	212.3	61.64	300.4	200.2	129	5.26	2.33	52405	240
9	NCS30_NPs	343.2	212.9	62.03	300.2	201.0	163	4.09	1.88	54228	243
10	NCS30_NPs	346.0	218.9	63.28	300.6	200.1	170	3.90	2.02	52519	243
11	NCS30_NPs	349.9	219.9	62.86	300.3	200.2	175	3.88	2.01	54358	245
12	NCS30_NPs	347.7	212.6	61.13	300.3	200.4	174	3.92	2.09	55400	246
13	NCS30_NPs	347.4	218.8	62.99	300.5	201.6	162	4.06	2.36	53870	242
14	NCS30_NPs	341.1	213.5	62.59	301.0	201.0	168	4.06	2.34	53544	244
15	NCS30_NPs	341.2	211.1	61.87	300.4	200.1	173	3.93	2.01	53447	191
16	NCS30_NPs	343.2	209.5	61.03	300.4	201.8	166	3.94	1.54	54423	247
17	Ref_Pb	351.5	199.5	56.78	300.8	200.7	125	5.24	1.68	65249	204
18	Ref_Pb	350.4	198.7	56.71	300.3	200.8	123	5.49	1.61	61651	241
19	Ref_Pb	346.3	211.2	61.00	301.6	200.6	126	5.46	3.81	56100	294
20	Ref_Pb	350.1	218.5	62.42	300.6	200.9	126	5.49	1.85	54944	244
21	Ref_Pb	349.9	218.7	62.51	301.5	200.0	138	4.84	1.98	55433	247
22	Ref_Pb	346.5	204.4	58.99	301.3	200.5	139	4.87	1.92	55319	245
23	Ref_Pb	351.9	212.1	60.29	302.0	201.5	139	5.09	2.07	55465	247
24	Ref_Pb	348.3	207.4	59.55	301.0	201.3	139	4.82	1.68	54423	251

Table 11. Summary of the data collected for a complete torque test of Group 3, petroleum jelly.

Run No.	Thread Compound	M/U Torque (ft-lbs)	B/O Torque (ft-lbs)	B/O to M/U Ratio	Upper Torque Curve Fit (ft-lbs)	Lower Torque Curve Fit (ft-lbs)	Points Curve Fit	Slope of Line (ft-lbs/deg)	Mean Square Error	Max Load [lbs]	Max Angle [degrees]
1	Ref_Pb	361.4	238.2	65.91	301.2	203.5	125	5.37	2.53	49683	197
2	Ref_Pb	364.0	236.4	64.95	302.1	202.6	128	5.74	1.89	49949	206
3	Ref_Pb	354.6	233.1	65.74	302.2	201.4	125	5.31	2.48	49576	226
4	Ref_Pb	348.2	241.5	69.36	300.3	201.6	129	5.72	2.59	49878	196
5	Ref_Pb	353.8	235.3	66.51	301.2	203.4	115	5.87	1.26	50477	188
6	Ref_Pb	358.0	240.1	67.07	302.1	200.3	120	5.68	1.85	50044	212
7	Ref_Pb	352.5	236.7	67.15	304.0	202.3	126	5.36	1.99	51146	186
8	Ref_Pb	359.1	228.9	63.74	300.1	201.1	118	5.71	2.06	49976	231
9	Petro Jelly	345.4	204.4	59.18	302.0	202.4	121	3.67	2.35	51755	212
10	Petro Jelly	352.7	208.6	59.14	301.3	201.8	130	4.16	2.03	51788	198
11	Petro Jelly	349.9	210.4	60.13	302.3	201.7	128	3.11	2.15	51429	190
12	Petro Jelly	349.9	205.4	58.70	305.1	202.3	127	3.62	1.54	51788	206
13	Petro Jelly	363.5	220.3	60.61	300.9	200.8	124	4.01	2.73	53255	243
14	Petro Jelly	346.9	207.8	59.90	302.6	202.4	129	3.58	1.79	52049	227
15	Petro Jelly	353.8	209.4	59.19	300.1	200.1	131	3.19	2.23	52391	189
16	Petro Jelly	355.5	213.4	60.03	302.6	202.4	128	3.26	1.19	51521	196
17	Ref_Pb	351.7	232.2	66.02	303.0	201.6	126	5.68	2.68	49355	206
18	Ref_Pb	351.2	229.9	65.46	300.7	201.7	127	5.83	1.97	49404	186
19	Ref_Pb	352.8	226.7	64.26	303.3	200.8	121	5.64	2.36	49828	193
20	Ref_Pb	350.7	226.2	64.50	302.3	202.2	126	5.86	2.74	50121	224
21	Ref_Pb	355.6	227.8	64.06	300.8	203.8	132	5.32	2.21	50854	183
22	Ref_Pb	359.6	231.5	64.38	301.8	201.1	128	5.41	1.64	50903	214
23	Ref_Pb	360.5	230.9	64.05	301.8	200.1	124	5.47	1.79	51229	201
24	Ref_Pb	359.0	237.3	66.10	301.2	202.3	129	5.68	1.66	50806	195

Table 12. Summary of the data collected for a complete torque test of Group 4, petroleum jelly + 2.3wt% a-ZrP.

Run No.	Thread Compound	M/U Torque (ft-lbs)	B/O Torque (ft-lbs)	B/O to M/U Ratio	Upper Torque Curve Fit (ft-lbs)	Lower Torque Curve Fit (ft-lbs)	Points Curve Fit	Slope of Line (ft-lbs/deg)	Mean Square Error	Max Load [lbs]	Max Angle [degrees]
1	Ref_Pb	361.0	245.8	68.09	300.3	200.3	123	5.27	1.86	44475	189
2	Ref_Pb	360.7	244.2	67.70	300.7	201.3	125	5.41	1.62	43906	176
3	Ref_Pb	348.1	236.0	67.80	300.1	202.2	126	5.22	1.26	44117	204
4	Ref_Pb	350.7	230.5	65.73	300.6	201.9	128	5.28	2.15	45109	168
5	Ref_Pb	354.5	235.5	66.43	301.5	203.6	124	5.38	1.48	46378	196
6	Ref_Pb	355.6	230.6	64.85	300.6	200.9	121	5.23	1.68	46459	207
7	Ref_Pb	358.9	231.5	64.50	300.3	202.6	129	5.18	1.98	47402	226
8	Ref_Pb	356.5	230.3	64.60	300.6	200.7	126	5.22	2.03	47809	234
9	PJ+NPs	357.6	237.5	66.41	303.1	201.8	131	4.21	2.14	46264	187
10	PJ+NPs	369.2	250.4	67.82	301.9	200.0	130	3.58	1.88	47972	196
11	PJ+NPs	358.4	248.7	69.39	303.5	201.5	128	3.88	1.76	48541	183
12	PJ+NPs	361.9	253.2	69.96	301.5	201.7	127	4.16	1.36	48330	224
13	PJ+NPs	354.2	246.8	69.68	300.4	201.9	126	4.26	1.27	47175	231
14	PJ+NPs	364.5	262.1	71.91	303.2	200.5	128	3.80	1.68	44215	202
15	PJ+NPs	358.7	251.9	70.23	307.4	203.9	132	3.75	1.92	43873	176
16	PJ+NPs	359.4	252.2	70.17	301.9	203.3	126	3.54	2.03	41092	189
17	Ref_Pb	359.9	254.5	70.71	303.7	203.0	121	5.54	2.04	41808	176
18	Ref_Pb	350.6	242.5	69.17	300.6	201.3	124	5.46	2.00	42344	208
19	Ref_Pb	353.4	239.6	67.80	301.8	202.2	126	5.52	1.81	46232	226
20	Ref_Pb	360.0	245.0	68.06	300.8	200.9	125	5.32	1.86	47777	249
21	Ref_Pb	347.7	234.5	67.44	301.1	200.7	127	5.24	1.92	46931	179
22	Ref_Pb	358.7	241.0	67.19	300.5	200.9	133	5.38	1.87	46850	179
23	Ref_Pb	360.7	240.9	66.79	301.1	200.0	122	5.47	1.56	44524	231
24	Ref_Pb	356.9	234.6	65.73	301.8	202.3	130	5.51	2.03	43808	208

The data in Table 9 through Table 12 display all relevant information collected during each of the test runs. The machine was set to rotate at 3 revolutions per minute (RPM) in the clockwise direction to “make-up” the samples to a certain torque limit. For all the test runs, the machine was set to stop at a make-up torque limit of 350ft-lbs so as to have the test samples run through a torque range of 200ft-lbs to 300ft-lbs in accordance with API 7A1 and API 5A3 standard procedure [58, 76]. Once the limit was

reached, the samples were separated, or "broken-out," by having the machine rotate in the counter-clockwise direction at 3 RPM. The data analysis requires that the slope of the make-up torque curve be calculated between 200ft-lbs and 300ft-lbs, which is shown in the "Slope of Line" column in the data tables. The standard testing procedure also requires that at least 120 data points be used to calculate the torque, this information can be found in the "Points for Curve Fit" column in the data tables. As shown in these columns, the number of data points varies for each test run. This can be attributed to the machine not stopping at the exact same torque limit for each of the runs. However, the machine slightly overshooting the limit is of no concern since the calculated slope values will be averages over several datasets.

From the collected data, the friction factor for each test group was calculated using the following equation:

$$FF = \frac{2 * S_2}{S_1 + S_3}$$

Equation 4.4

where S_1 is the average slope of the Make-Up curves for the first 8 runs of the reference compound, S_2 is the average slope of the Make-Up curves for the thread compound being investigated, and S_3 is the average slope of the Make-Up curves for the second 8 runs of the reference compound. The friction factors for each grease compound group are listed in Table 13.

Table 13. Summary of the calculated slopes for each data set and the calculated friction factor for each group.

Grease Compound	S_1	S_2	S_3	Friction Factor
Group 1	3.56	3.49	3.45	0.996
Group 2	5.26	3.97	5.16	0.763
Group 3	5.60	3.58	5.61	0.638
Group 4	5.27	3.90	5.43	0.728

4.4 Data analysis and discussion

As mentioned before, the friction factor is a ratio that relates the performance of a grease formulation to that of a grease with known performance. This means that the closer a friction factor is to 1.0, the more comparable its performance to the standard reference. For this investigation, all four test groups were evaluated against the API standard 60wt% Pb compound. This compound has a documented friction coefficient of 0.067 and well document to withstand the high temperature and high pressure demands of deep well oil drilling [64].

Analyzing the data from Table 13, it is clear that the best performing compound was the pure NCS-30 (Group1). This result is expected since NCS-30 is a compound specifically formulated to meet the friction demands of the drilling process. However, when iron oxide additives are incorporated into the compound (Group 2), a significant drop in performance is seen. The 23.4% reduction in frictional performance can be attributed to the nature of iron oxide particles. As mentioned before, iron oxides are normally formed through a chemical process or though the wearing of the steel material. These oxide particles have a high hardness and as a result will cause increased wear at

the interface and also hinder the flow of the lubricant. This is evident by the reduced friction factor.

Test Groups 3 and 4 consist of petroleum jelly compounds. Petroleum jelly is not typically used for industrial applications, but it has been shown to be a good base lubricant to evaluate various additives [77-79]. It is a clean base lubricant that does not contain any additives, unlike NCS-30 which has numerous metallic and non-metallic additives. By mixing a single type of additive into the petroleum jelly, any changes in performance can be directly attributed to that additive. The friction factor for pure petroleum jelly (Group 3) is relatively low compared to the pure NCS-30. As petroleum jelly was not designed to perform under high contact pressures and stress levels, the poor performance is expected. However, when 2.3wt% a-ZrP nanoparticles are added, the friction factor increases about 14%. This increase in performance can be attributed to the nature of the additive. The a-ZrP nanoparticles used in this study have a disc-like shape and are on the order of 100nm in diameter. The disc-like shape allows for the particles to easily slide against each other. Likewise, the flat disc shape combines with the strength of the material will help to carry the applied load across the mating surfaces. In addition, a-ZrP has weak Van der Waals forces that keep them bonded together in small groups [80-82]. The weak bonding among the discs allows them to more readily separate when a shear forces is applied, which is the case for the test procedure. It has been documented that adding a-ZrP to base oils will decrease its friction coefficient and decrease the overall viscosity of the mixture [80]. The results of the present study confirm prior findings for this additive.

4.5 Surface analysis

The metal test specimens from the evaluation of grease compound Groups 1-4 were further analyzed at the surface level. All test specimens were characterized using optical microscopy and interferometry. The testing equipment used in this study can be seen in Figure 25, along with their respective imaging results.

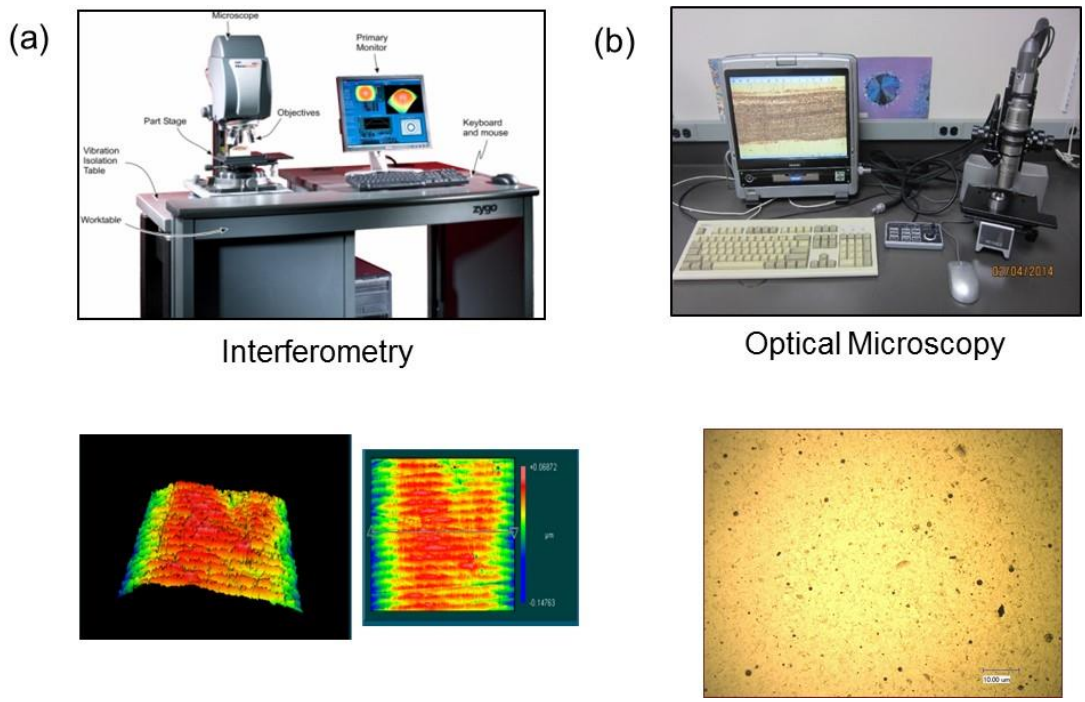

Figure 25. The (b) Zygo interferometer and (a) Keyance optical microscope used to evaluate the surface of the metal test specimens, with examples of their respective resulting images.

Performing a surface analysis before and after a test will further validate the performance of the grease. A well performing grease will leave little to no abrasions on

the surface and remain relatively smooth as in the beginning of the test. The goal of the surface analysis was to observe for galling on the samples. For all tests performed on the four grease samples, galling was not observed. An example of a typical test specimen surface is shown in Figure 26.

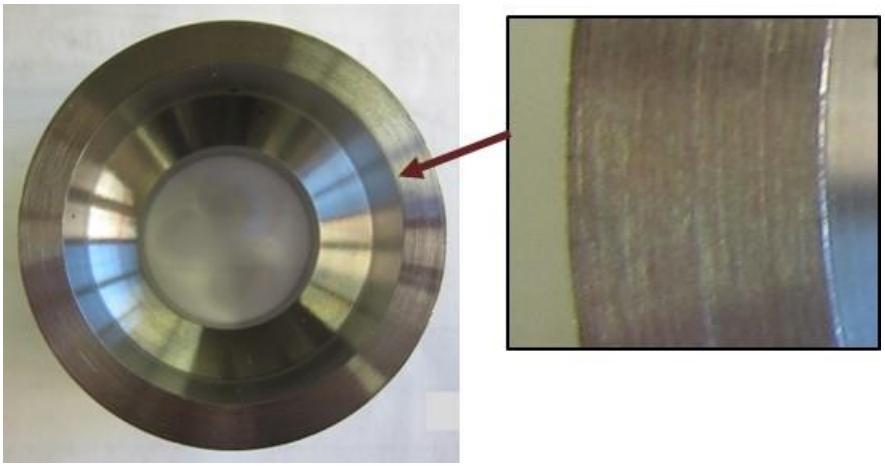

Figure 26. View of a test specimen surface after a friction experiment performed using the NCS30 grease group.

As shown in the figure, after running a friction experiment with NCS30 grease group, light surface roughness was observed. The surface roughness was located along the rotational direction along the metal test specimen. The change in surface roughness was not significant and did not have an effect on the friction results. The number of tests performed using the same grease group and same metal test specimens (i.e. 24 total runs) showed that there was no statistical variation in friction.

CHAPTER V

EFFECTS OF GEOMETRIC FACTORS OF FRICTION

This chapter will discuss the geometries of the point, line, and area contact tribotests discussed in the previous two chapters. A geometric relationship will be established to compare contact pressure with friction performance.

5.1 Contact geometry

As discussed in Chapters 3 and 4, the interface of the material contacts will undergo a Hertzian contact analysis. This method assumes that the mating materials have a perfectly smooth surfaces and each have some elastic properties [49]. Having perfectly smooth surfaces is important as it implies complete contact between each of the materials, without significant gaps in between. The elastic property analysis asserts that the materials will undergo some form of elastic or plastic deformation as a result of an applied force. For the case of a point, or zero dimension (0D), contact the ball bearing will deform at the initial contact point. The deformation will result in the actual contact region being circular, with some radius, a. For the case of a line, or one dimensional (1D), the initial contact will deform in two directions. The deformation will cause the line to transform into an ellipse with some major axis, a, and minor axis, b. Essentially, the 0D and 1D contact schemes used in this research will have some two dimensional aspect as a result of the material deformation. The two dimensional (2D), area contact tribotest used in this research will also undergo slight deformation at the interface. However, the additional area contribution is not as significant as the initial area contact.

A summary of the geometrical configurations for each tribitest are listed in Figure 27, along with the corresponding contact area region.

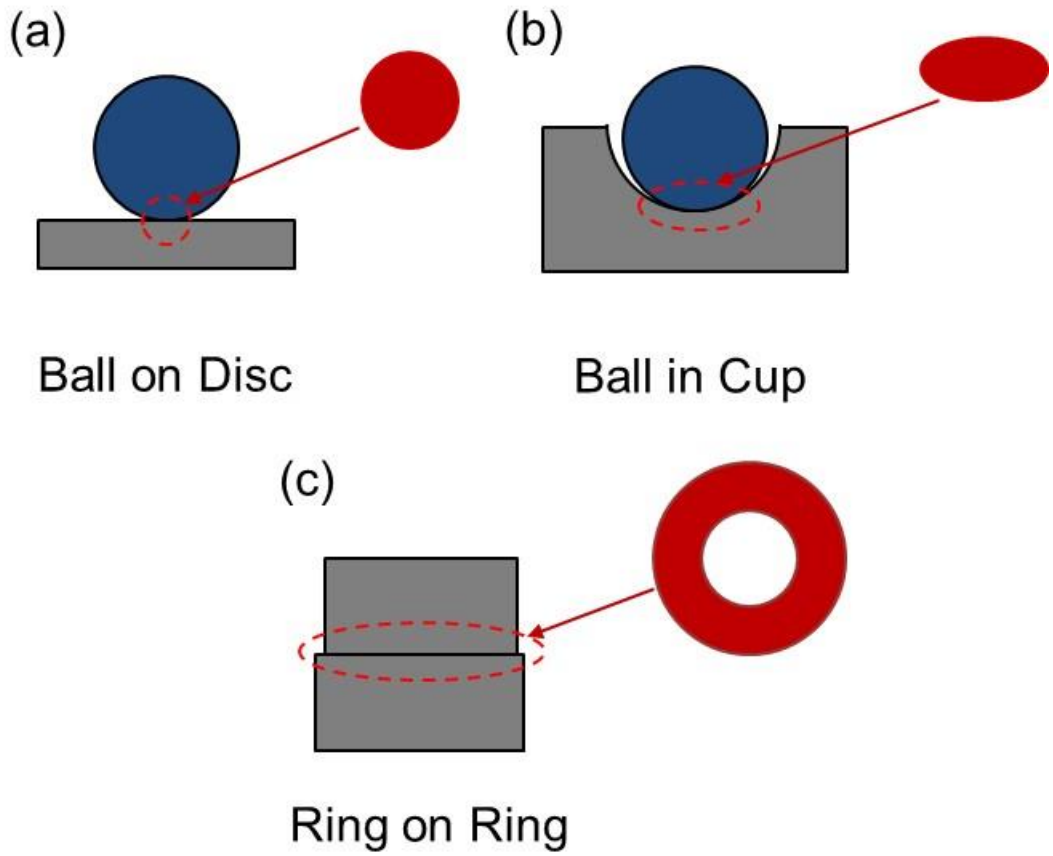

Figure 27. Schematic diagrams showing (a) point (0D) contact, (b) line (1D) contact, and (c) area (2D) contact geometry.

For lubricated contact regions, the lubrication regime will experience different types of separation due to the presence of the lubricant [83]. For a standard liquid, or oil, lubricant analysis the performance of the materials may be characterized using a Stribeck Curve [7]. A Stribeck curve is a plot of friction coefficient versus a non-dimensional lubrication parameter. The non-dimensional parameter may be represented by the following equation:

$$S = \frac{\eta V}{P}$$

Equation 5.1

where η represents the viscosity of the liquid lubricant, *V* is the sliding speed of the system, and *P* is the applied load. The coefficient of friction is likewise a non-dimensional parameter that is used to evaluate the frictional performance of two interacting materials. This quantity may be determined using the following equation.

$$\mu = \frac{f}{P}$$

Equation 5.2

where *f* represents the friction force, and *P* is the applied load as mentioned previously for the lubrication parameter. For purposes of this research, the coefficient of friction

will be used to evaluate the effectiveness of the grease being used between the sliding contacts.

As mentioned above, liquid lubricants are commonly analyzed using a Stribeck Curve. However, semi solid lubricants such as grease may not be analyzed using the same type of curve. Many issues arise when trying to uses the same analytical method as, for example, an oil. For one, grease does not flow like an oil, and the additives and complex mixtures will cause the grease to behave inconsistently. However, the lubrication regimes presented by the Stribeck Curve may be used for a baseline comparison. Three distinct regimes may be observed: boundary, mixed, and hydrodynamic lubrication. The three regimes are illustrated in Figure 28.

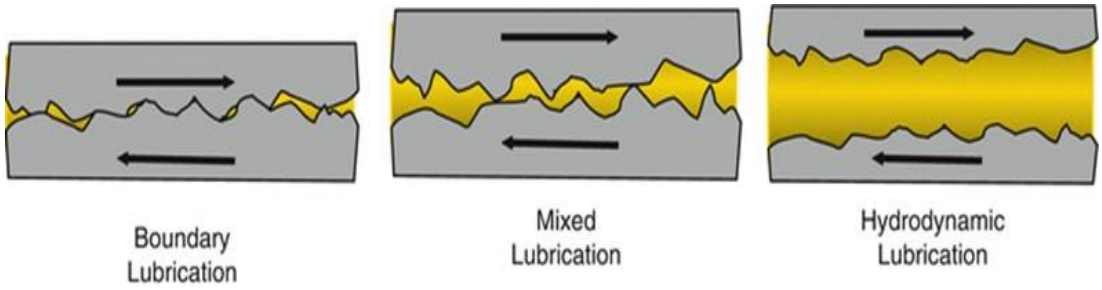

Figure 28.Schematic diagrams of the three primary lubrication regimes represented by a Stibeck Curve analysis.

As the images in Figure 28, show each region is characterized by how much separation exists between the mating surfaces. In boundary lubrication there is mostly surface to surface contact, with only slight lubrication existing in between the asperities.

As mixed lubrication is approached, the surfaces become more separated and a full fluid lay begins to form. Hydrodynamic lubrication represents complete separation of the mating surface and a full fluid flow in between. In general, the more the mating surfaces come into contact, the higher the friction coefficient will be. Thus, boundary lubrication represents a higher friction scenario. However, in hydrodynamic lubrication friction is influenced by the fluid properties of the lubricant. Therefore, low friction may be observed for low sliding speeds, but increase as the speed is increased to produce drag forces by the fluid. For a lubricated condition, the separation of the mating materials will greatly depend on the applied load and the ability of the lubricant to carry the load [84, 85].

For the case of grease, due to its high viscosity and incorporation of additive particles the load carrying capabilities will vary. However, it is accepted that the vast majority of greases have better load carrying capabilities than liquid lubricants [86]. In addition, a Hertzian contact analysis will still be possible under lubricated conditions. The load carried by the lubricant will vary based on the area of the contacting region [50]. Essentially, at the highest contact region will contain the least amount of lubricant while the remaining contact region will have a fairly even distribution. Grease will become entrained within the contact region regardless of the area [86-88].

5.2 Geometric analysis

Through a Hertzian contact analysis for two mating material, it is important to take the elastic properties of the materials into consideration when determining the actual contacting area. A relationship between the elastic modulus and the ratio of transverse strain to lateral strain (Poisson's ratio) of the two materials may be expressed through the following equation.

$$\gamma = \frac{(1 - v_1^2)}{E_1} + \frac{(1 - v_2^2)}{E_2}$$

Equation 5.3

where *E1* and *E2* represent the modulus of elasticity of the static and dynamic material respectively, and *v1* and *v2* represent the Poisson's ratio of the static and dynamic material respectively. Likewise, under Hertzman analysis, a geometric relationship must be established for the curvature of the mating materials. This takes into account the radii of each mating material. Essentially, it is understood that the amount that a curved surface will deform and make contact with the mating surface will depend on the radius of curvature. In the case of a flat surface, the radii of each surface will be zero and will not need to be accounted for. A diagram of the three contact geometries used in this research are shown with the corresponding geometric parameter, K, in Figure 29 below.

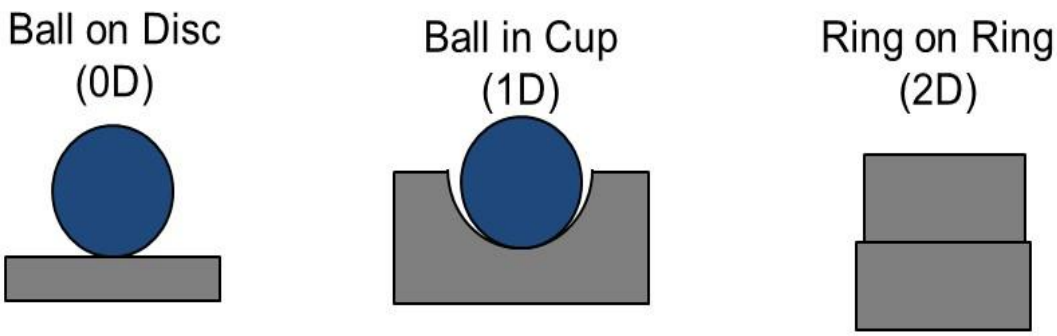

$$K_0 = \frac{1}{\frac{1}{R_1} + \frac{1}{R_2}} \qquad K_1 = \frac{1}{\frac{2}{R_1} - \frac{1}{R_2} + \frac{1}{R_3}} \qquad K_2 = 1$$

Figure 29. Schematic diagram of the three contact geometries used in this research, along with the corresponding geometric parameter, K.

As Figure 29 shows, the parameter K is not constant for all types of configurations. The values for each of the radii shown are better explained in Chapter 3 and 4. Since the ring on ring configuration consists of two flat materials, there is no need to take curvature into account. In this case the value for K will be equal to 1. Now that the elastic and geometric constraints have been established for each configuration, the effective values for the contact geometry may be found. The corresponding geometric analysis for each of the tribotest configurations are elaborated in greater detail in Chapters 3 and 4. A summary of the governing equations are listed in Table 14.

Table 14.Summary of the three contact regions experienced by the tribotesting methods discussed in this research, along with the corresponding governing parameters and resultant contact area.

Contact Region	Parameter	Area
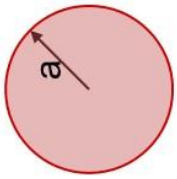	$a = \sqrt[3]{\frac{3}{16} F \frac{\gamma}{K_1}}$	$A = \pi a^2$
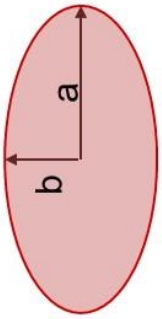	$a = 1.145 n_a \sqrt[3]{F K_2 \gamma}$ $b = 1.145 n_b \sqrt[3]{F K_2 \gamma}$	$A = \pi a b$
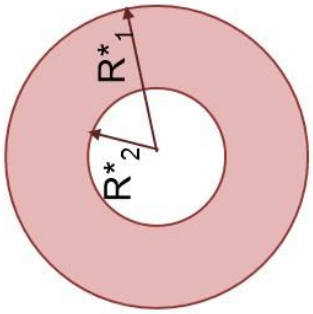	$R_1^* = R_1 + \gamma K_3$ $R_2^* = R_2 + \gamma K_3$	$A = \pi[(R_1^*)^2 - (R_2^*)^2]$

From the governing equation set by the Hertzian analysis, the corresponding contact pressures may be determined. The measurement of pressure may be represented as the ratio between the applied loading force and the effective contact area. Under a Hertzian analysis, the contact pressure is multiplies by a factor of 2/3 to account for the complex stress distribution occurring beneath the surface [89]. Essentially, the maximum contact pressure will occur along the center of the contact area and be less along the perimeter [50, 90]. Although a universal pressure equation is not available for all contact scenario, one may be extrapolated from the analysis performed on the contact regions used in this research. The general contact pressure equation will take the form of the following:

$$P = \frac{3F}{2} * \frac{1}{A^*}$$

Equation 5.4

where F is the applied force, and A* represents the effective contact region. In this case, the effective contact region, or area, represents the geometry of the test configuration. Based on the aforementioned equation, it is clear that the contacting pressure will have an inverse relationship to the geometry; whether it be zero, one, or two dimensional. Through the derived pressure equation above, it is possible to plot a pressure distribution at constant load values to see how it is influenced by contact area (Figure 30).

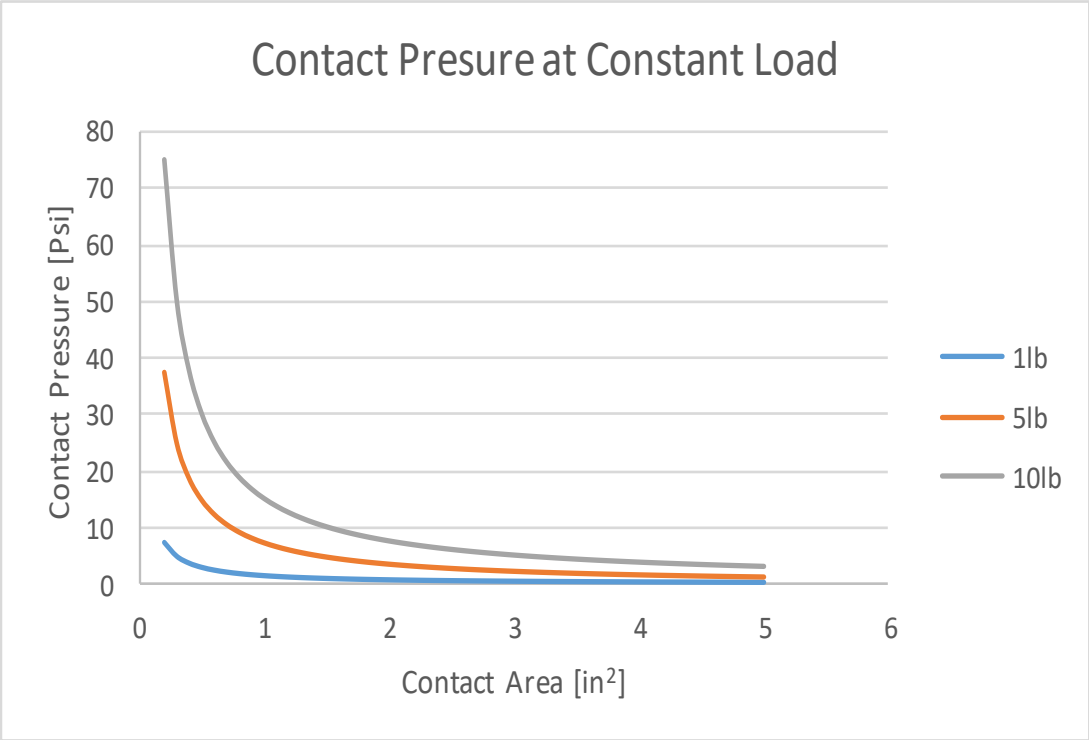

Figure 30. Plot of pressure distribution at constant load versus effective contact area.

As shown in Figure 30, the contact pressure will decrease at an exponential rate as the effective contact area is increased. Higher loads will yield higher contact pressures, as expected, but once the effective area increased to a certain point the effect of load is not as significant. This trend lends to the notion that larger geometries will support greater loads and thereby reduce the friction between sliding surfaces. In addition smaller contact pressures will allow for a more consistent distribution of lubricating grease between the surfaces. Again, this will allow for a decrease in friction and better performance.

As discussed in previous chapters, the contact geometries of each of the three tribitests used in this research were used to evaluate the frictional performance of four different grease mixtures. Due to the limitations of the two dimensional, area contact apparatus, experiments using it were only conducted at room temperature. Unlike the point and line contact experiments which also underwent both high and low temperature testing. Therefore, only the room temperature experiments will be evaluated against the geometric configuration. A plot of friction coefficient versus the contact type: 0, 1, and 2 dimension is shown in Figure 31 below.

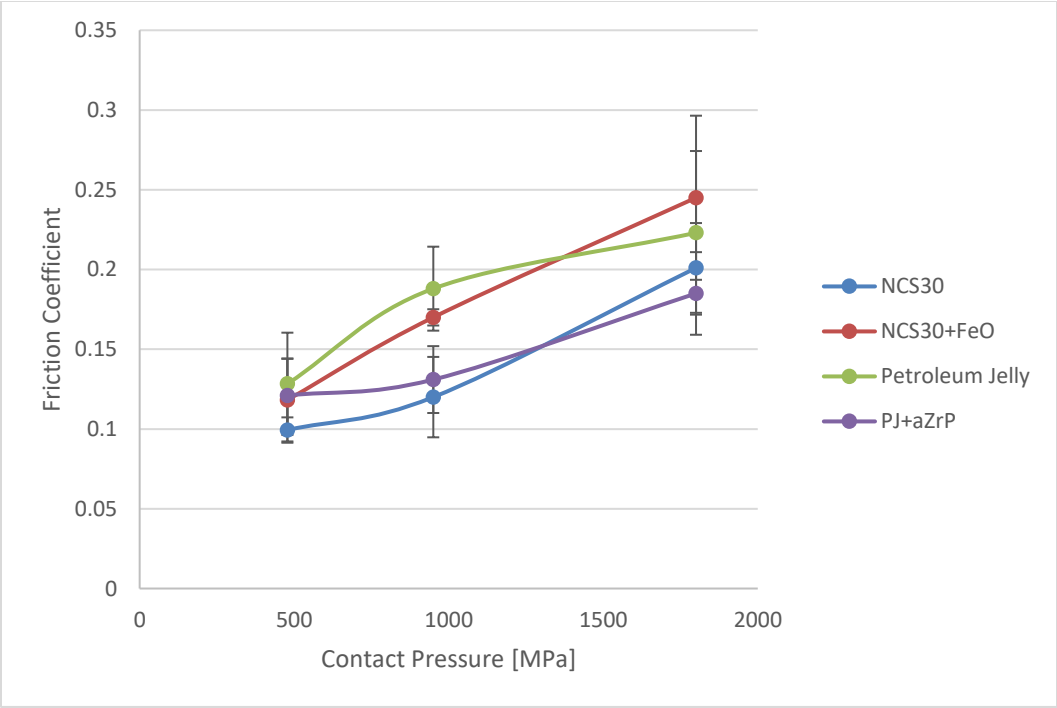

Figure 31.Plot of friction coefficient versus contact geometry type for the four grease groups under investigation.

As the plot in Figure 31 shows, there is a trend for the friction coefficient to decrease as the contact pressure decreases. The highest contact pressure is experienced under the point contact experiment, while the lowest is experienced by the area contact experiment. This trend lends well to the behavior of the pressure distribution mentioned above, and shows that the performance of grease is greatly affected by the contact geometry. In other words, a proper analysis of grease would require that it be tested in a configuration similar to that of its intended use. Testing NCS-30, a grease made for use in the oil and gas industry to connect drill pipe together, using a pin-on disc tribometer would not provide accurate information. Under a pin on disc setup, the friction coefficient is relatively high for all grease groups, which indicates that boundary lubrication is taking place. As the geometry is increased more lubricant will become present within the contacting region, thereby allowing for mixed or hydrodynamic lubrication. The greater amount of grease is present, the lower the friction and the better the overall performance.

CHAPTER VI

DIRECT PROBING OF LUBRICANTS

This chapter will provide information on methodologies that allow for in situ monitoring of lubricating systems, with an emphasis on lubricants.

6.1 Experimental design and configuration

The term "*in situ*" is a Latin phrase that translates to "in position," or "in place." When related to a scientific testing environment, it refers to the ability to monitor a particular phenomenon without having to remove anything from the system being investigated. Performing in situ analysis on a system has significant advantages over *ex situ* analysis since it allows for a true monitoring of what is happening at any given time. *Ex situ* refers to testing procedures that require analysis after a test is completed. In the case of tribology, an example of ex situ analysis would be a typical wear analysis of the surface that is performed after the friction test.

In regards to the tribotesting methods discussed in this research, they all provide *in situ* monitoring of some form. For the point and line contact tribotests, the friction coefficient, applied load, and friction force are measured in real time throughout the length of the test. The area contact galling resistance test machine allows for *in situ* monitoring of the applied load and resultant torque during the course of the test. However, each of the aforementioned testing methodologies cannot give accurate representation of what is occurring within the lubricant or at the surface level. All lubricant and surface analysis must be performed *ex situ* in one of many characterization

methods. Wear analysis for example, is performed by using a combination of microscopy and profilometry after a tribotest is performed. Although newly developed testing configurations can allow for in situ wear monitoring, the test equipment is not widely used. The lubricants can be analyzed using various spectroscopy methods to note of any chemical or compositional changes after a tribotest.

For an *in situ* analysis of lubricant flow, some methods have been developed by other researchers which provided various results [21, 91, 92]. These methods involve replacing a metal component with a clear glass pane somewhere near the working surfaces. For a journal bearing grease analysis for example, the end plate of the bearing may be replaced with a glass one [21]. Another example would be to replace the substrate material of a pin-on-disc configuration with a clear glass plate. The incorporation of a glass section to a test apparatus allows for a visual inspection of the tribosystem. Having a window allows for different optical measurement devices to be incorporated. A high speed camera may be used to record the motion of the grease and record any wear that forms over time [93]. A thermal imaging camera maybe used to record any temperature changes that occur. Still, more complex analysis may be carried out by adding tracer particles into the lubricant that may be tracked using fluorescence [92].

While all these methodologies have proven useful, they only have practical use for systems that have a large separation for which the lubricant to flow; such as in a bearing. Thin lubricant films cannot be accurately monitored with these methods. A new *in situ* method that can visualize lubricant flow is needed.

6.2 Digital imaging and tomography approach

One of the most common methods to visually inspect the internals of an object is through computed tomography (CT). In the medical industry a CT scan is a widely used practice that is used to diagnose a range of ailments within a patient. It is a non-invasive and non-destructive method that produces high resolution images that lend to more accurate medical diagnosis. A schematic diagram of a typical CT scan is shown in Figure 32.

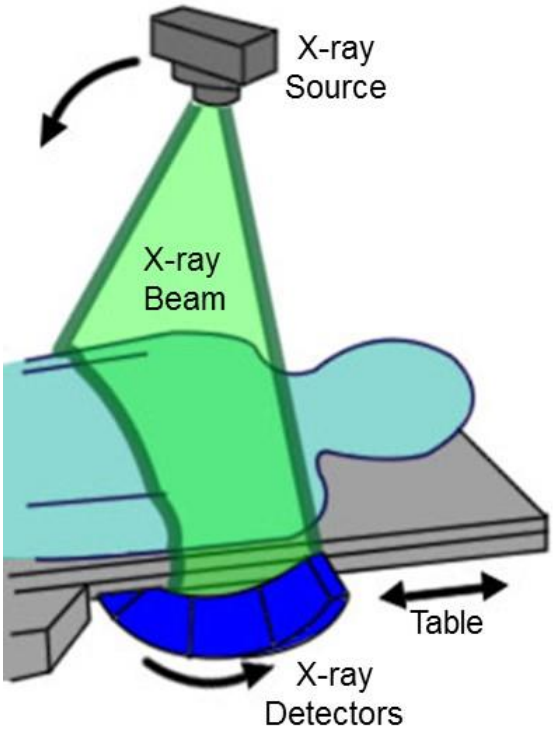

Figure 32. Diagram of the procedure and basic components of a medical CT scan.

The two primary component of a CT machine are the x-ray source and a series of detectors. The patient is set on a motorized table along the central axis in between the x-ray and the detectors. The x-ray source is set to a particular energy level and allowed to pass through, or scan, the patient. The light waves that pass though or interact with the object are then collected by the detectors and converted into an image. The x-ray source and the detectors are simultaneously rotated around the patient so as to capture information at all angles. Once one segment of the patient is scanned, the table is moved forward and the next section is scanned. The resultant images offer a highly detailed mapping of the internal structure of the object that was scanned. The individual scanned sections show an orthogonal cross sectional view of the object. Each of the orthogonal views may also be combined to render a full three dimensional image of the object. One critical aspect of this imaging procedure is that the patient must remain completely stationary while the scan is taking place. Otherwise, the resulting images will be blurry or have artifacts. The time required for a full body scan will depend on the patient.
The same CT scanning technology may be applied to a wide array of objects, including inorganic materials [94]. However, the image resolution for standard CT scan is in the millimeter range and is not suitable for imaging, for example, small surface cracks in a metal component. In order to images smaller feature in the micron and sub-micron range, micro computed x-ray tomography (μ-XCT) may be used.

Depending on the configuration of the equipment used, a synchrotron based μ-XCT can yield two dimensional (2D) orthogonal views at resolutions within the micron range [95, 96]. The high quality 2D orthogonal views may then be used to generate fully

three dimensional (3D) reconstructions of the entire scanned object. In contrast to a medical CT scanner, a μ-XCT scanning system can be used for a wide array of materials through the adjustment of the monochromatic X-ray energy [97, 98]. This method of tomography is well suited for imaging small features such as imperfections within electronic devices and small industrial components. Due to its high accuracy imaging, μ-XCT is capable of detecting micro cracks inside metal parts, and faults in integrated circuits. In previous research studies, μ-XCT was used to investigate the localization of nanoparticles within mealworms and cabbage leaves [99, 100]. Through careful handling of the organic materials, the nanoparticles within the cells and tissues were able to be clearly identified. Therefore, this type of system is well suited to image the shear behavior of grease and various additive particles. The experience gained from those previous studies will be applied to the investigation of a lubricant using μ-XCT. The work moving forward will be the first time that an investigation of this nature will be conducted.

6.3 Feasibility of tomography

To prove the feasibility of tomography, we, the Surface Science Group at Texas A&M University conducted experiments on cockroaches that were fed on nanoparticles. One such study involved the investigation of silver (Ag) nanoparticles inside a cockroach.

Synchrotron-based micro-tomography is the ideal technique to study metallic NPs within an insect. The requisite optimal energies for imaging metallic NPs are well within the optimum range of the x-ray beam-line. Thus, placing an insect within the

beam-line to image NPs therein will offer greater insight into their physiological interactions. Specifically, live Discoid cockroaches (*Blaberus discoidalis)* were injected with silver NP solutions near the back of the head. Enough time was allowed after the injection for the insects to metabolize the NPs before fixing them for experimentation. Synchrotron x-ray micro-tomography was then conducted on the roaches to produce 2D orthogonal and 3D rendered images that were used to determine the locations of the Ag NPs. Ag NPs were produced using our protocols developed by a standard synthesis method [101]. The average diameter of Ag NPs was ~70 ± 20 nm. Assuming that the NPs were spherical in shape, the mass of a single NP was calculated to be 1.883×10^{-9} µg with a diameter of 70 nm.

Computer tomography was conducted at beamline 8.3.2 of the Advance Lights Source (ALS) of the Lawrence Berkeley National Laboratory (LBNL). Monochromatic light at 25.25 keV and 25.75 keV was used to obtain radiographs of the Discoid cockroach. Radiographs were collected at a pixel size of 0.004458 mm with a 2× optical lens focused on a scintillator. The cockroach was rotated 360° in 0.5° increments with a bright field image every twenty steps for intensity calibration.

Figure 33 shows a fully reconstructed 3D image of a cockroach on the left, and a reconstructed cockroach with the Ag NPs superimposed in red.

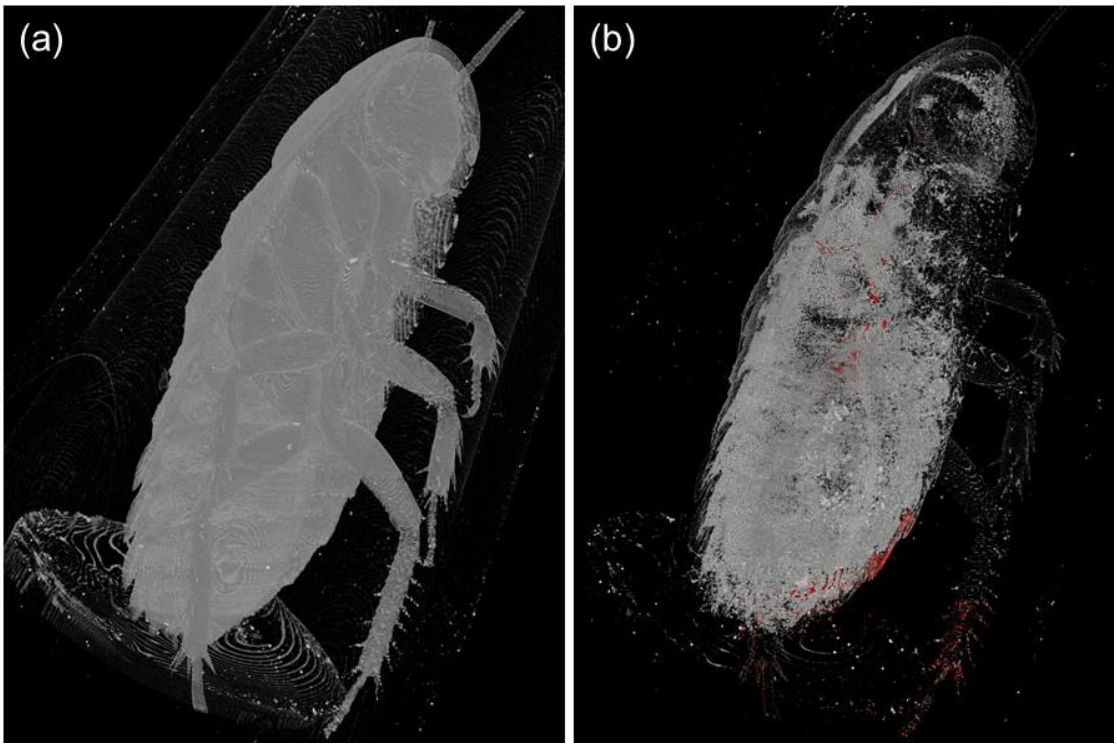

Figure 33. Complete three dimensional reconstruction of the Discoid cockroach. (a) The full roach showing the outline of the plastic tube and capillary wax at the bottom. (b) The full roach made more translucent, with the AG NPs superimposed within the body.

The small, red agglomerations were found by subtracting the entire roach dataset collected at 25.25 keV from the one collected at 25.75 keV. The result was a dataset that only showed bright spots for elements with higher attenuation coefficients; in this case Ag. The dataset was then colored red and superimposed within the 25.25 keV dataset for visualization. Figure 34 shows a close up view of the same roach, with Ag NPs seen as red agglomerations within the thorax.

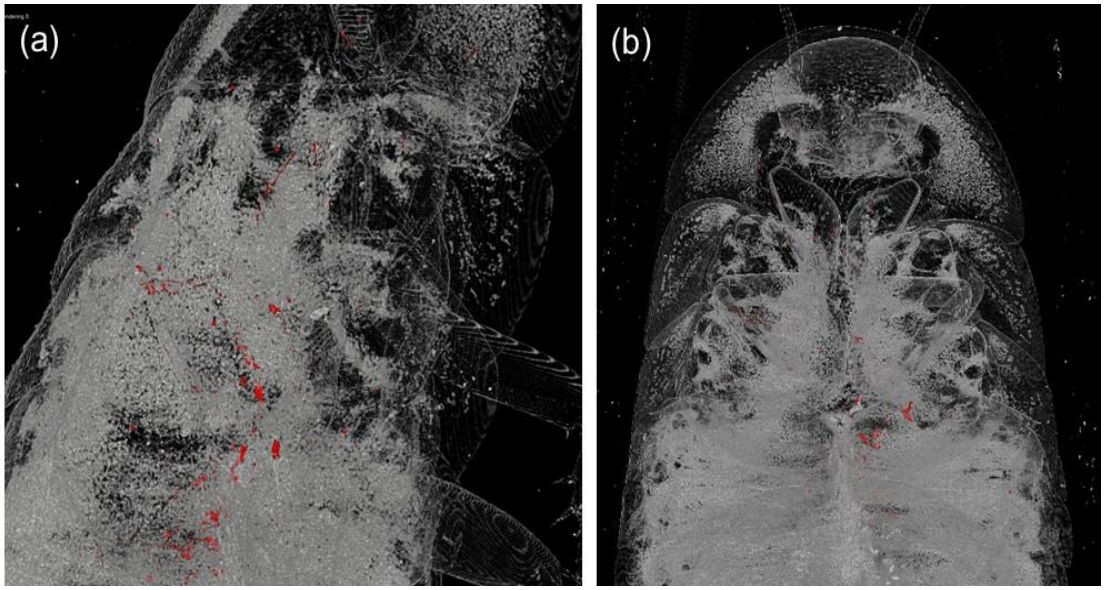

Figure 34. Close up views of the AG NPs (in red) within the cockroach body. (a) View of the right side of the body, showing the top thoracic segments. (b) Front view of the top thoracic segments with NPs superimposed.

Figure 33 and Figure 34 also show various details within and around the cockroach, such as internal organs, organ and cuticle boundaries, and the outline of the plastic tube used to hold the roach in place.

Synchrotron-based micro-tomography clearly indicates interactions of NPs within the cockroaches. Using the knowledge gained from this tomographic study on cockroaches, a new in situ methodology to analyze lubricating greases was developed. Details of the new methodology will be discussed in the next section.

6.4 Viscometer device for tomography

The visualization of a lubricating grease has not been accomplished before using beamline micro tomography. As such, a testing setup does not exist and needed to be developed. The goal of this research is to take images of a grease as received, then take another image of the same grease after a shear force is applied to it. By comparing the two sets of images, the behavior of the grease and any additive particles will be revealed. In order to test the feasibility of imaging particle additives in grease, a simple setup was first devised. The setup consisted of two concentric polyamide plastic tubes affixed to the rotational sample table of the μ-XCT, along the central z-axis. A sample of grease with additives was then placed in between the concentric tubes. An image of the tubes can be seen in Figure 35.

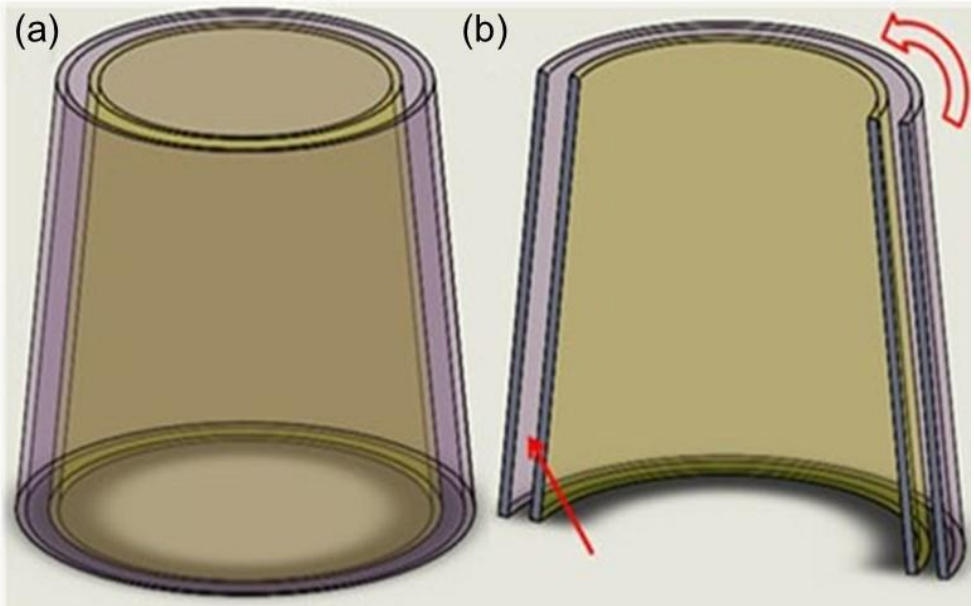

Figure 35. The concentric tubes for shearing grease. (a) Diametric view and (b) Section view of the tubes. The grease samples were deposited within the gap between the tubes (red arrow). The curved arrow indicates the rotation direction.

The goal of this experiment is to image a grease mixture within the annular gap of the cylinders, apply a shear force, then image it again to see how the particles interacted. For this particular setup, a mixture of NCS-30 and 2.3wt% Fe3O4 was imaged before and after shear. Due to the simplicity of the setup, the shearing was applied by hand through rotation of the inner cylinder for one minute. Using this methodology, the exact shear stress could not me calculated. Additionally, the tubes were affixed with adhesive putty to the rotational table. The tubes were placed by eyesight, which meant that they did not sit directly along the central axis, and likewise did not sit at the same location in between sample sets. However, the end results showed that the particle additives within the grease could easily be identified within the grease.

The results of this experiment, as well as the testing parameters used will be discussed in later sections.

Given the success of the feasibility experiment, the process of shearing and imaging grease was improved upon. For the next study, a small viscometer-like device was designed and fabricated to more precisely apply a shear force to the grease. In addition, the device was specifically built to sit directly in the center of the rotational axis of the μ-XCT sample table. This improvement allowed for more precise and repeatable imaging from one setup to the next. The tubes did not need to be removed in order to be sheared, meaning that the positioning remained the same from scan to scan.

The new testing rig consists of a rotating inner cylinder and a stationary outer cylinder made from polyamide plastic tubes. Polyamide tubes are necessary as they will appear “transparent” under x-ray and allow for an unobstructed view of the grease mixture. The inner cylinder is connected to the shaft of a 2 phase stepper motor and a rotary encoder. The speed of the motor is electronically controlled, while the encoder measures the rotational speed of the inner cylinder. A closed loop control system was used to supply a sufficient amount of torque to maintain a set motor speed over the test period. A diagram of the rig design can be seen in Figure 36.

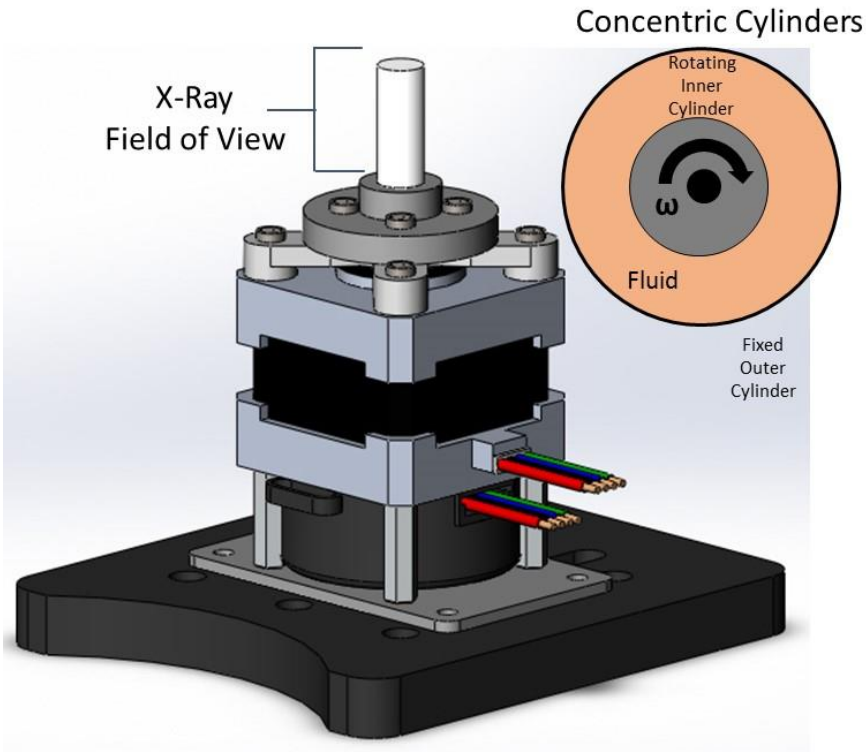

Figure 36. Diagram of the concentric cylinder testing rig used to shear the grease/nanoparticle mixture.

The entire rig is situated such that the rotational axis of the tubes sit along the central axis of the μ-XCT sample table as shown in Figure 37. The outer diameter of the stationary outside tube is 4mm, which is less than the 5mm field of vision (FOV) of the microscope used to perform the imaging. This configuration will allow for a uniform scan of the entire annular gap between the cylinders, and a clear image of the grease and NP mixture.

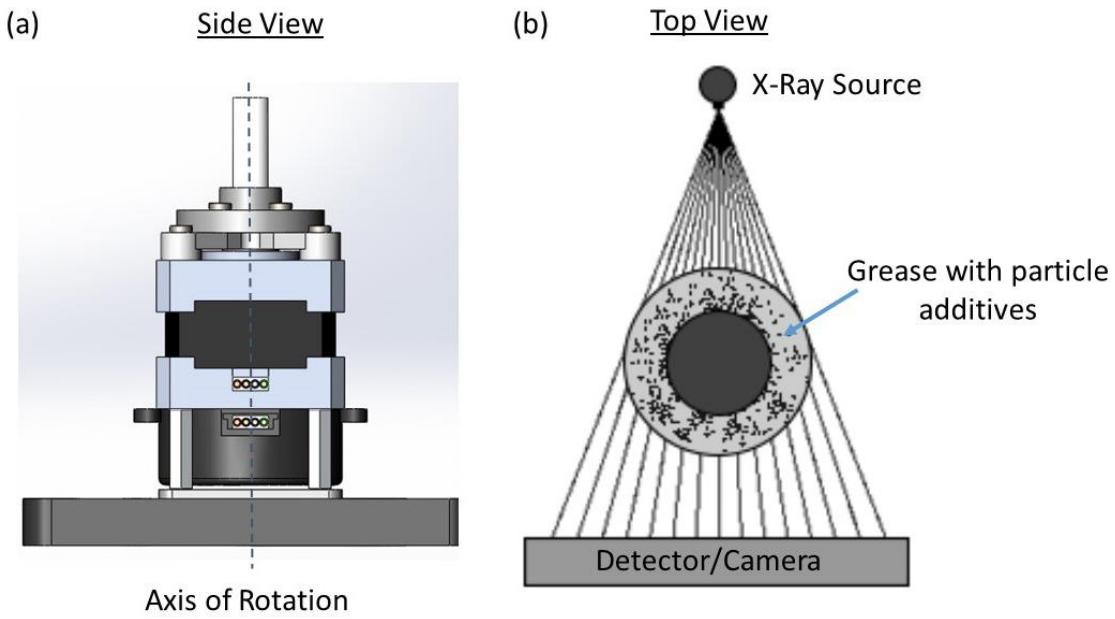

Figure 37. (a) Side view of the testing rig, indicating the axis or rotation, and (b) Top view of the concentric cylinders with grease/additive mixture, illustrating the scanning configuration.

The concentric cylinder device was calibrated prior to placement into the beamline so as to minimize error and simplify the test procedure when placed within the beamline. Based on the specifications of the motor used, a constant torque of 9.5 N-cm was established for the grease sample at a rotational speed of 25 revolutions per minute (RPM).

To understand the behavior of grease, we first estimate the value of the shear stress. The concentric cylinder testing rig was designed based on the mechanics and operation of a standard rotating cylinder viscometer. Based on the geometry and orientation of the testing rig, the diagram shown in Figure 38 was established.

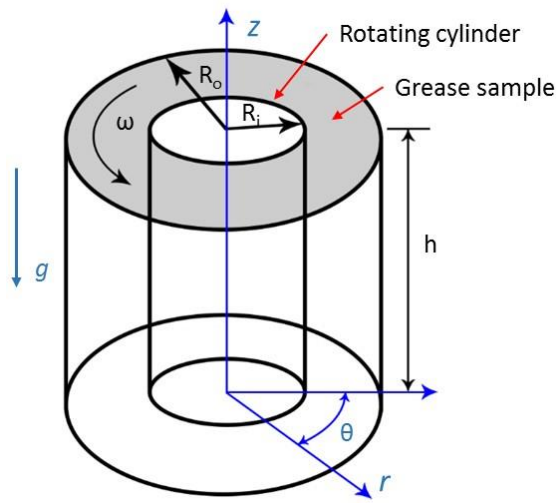

Figure 38. Diagram view of the concentric cylinder testing rig, indicating key parameters in cylindrical coordinates.

For this configuration, the annular gap width will be 0.05mm. Since the gap is small, and the duration of the test was relatively short, it will be appropriate to neglect the effects of gravity on the grease sample. The shear stress analysis on the grease will follow the Herschel-Bulkley rheological model, which has been shown to be a good approximation for the behavior of petroleum jelly [79, 102]. The equation of motion of the system can be expressed as the following:

$$\rho \frac{Dv}{Dt} = \rho \frac{\partial v}{\partial t} + \rho (V \cdot \nabla) v = \nabla \cdot \tau + \rho F$$

Equation 6.1

where D/Dt is the material derivative, v is the velocity vector, τ is the stress matrix, and F represents the body forces. As mentioned above, due to the small gap width, the body

force of gravity acting on the grease in the axial direction can be neglected. Here, we will assume a one dimensional flow. Hence in cylindrical coordinates, $v = v_\theta(r)$ and $v = v_r = v_z = 0$. Due to symmetry in the angular direction, $\frac{\partial}{\partial\theta} = 0$. Similarly, the symmetric stress matrix will have non-zero components at $\tau_{\theta r}$ and $\tau_{r\theta}$. Equation 1 can be reduced to the form:

$$\frac{\partial(r^2\tau_{\theta r})}{\partial r} = 0$$

Equation 6.2

Integrating this equation will give the governing momentum equation in the θ-direction as:

$$\tau_{\theta r} = \frac{C}{r^2} = f(r)$$

Equation 6.3

where $\tau_{\theta r}$ is the shear stress, and C is a constant. A generalized form for Equation 6.3 for a Newtonian fluid can be expressed as:

$$\tau_{\theta r} = \eta(\dot{\gamma})r\frac{d}{dr}\left(\frac{v_\theta}{r}\right)$$

Equation 6.4

where η is the viscosity, and $\dot{\gamma}$ is the shear rate. For a one dimensional flow, which is assumed for our setup, the shear rate can be simplified to the following form:

$$\dot{\gamma} = r\frac{\dot{d}}{dr}\left(\frac{v_\theta}{r}\right)$$

Equation 6.5

Integrating with respect to the inner and outer radius of the annular gap will yield the equation for the shear rate applied by rotating the inner cylinder. The equation will take the form:

$$\dot{\gamma} = \omega\frac{2R_i^2R_o^2}{(R_o^2 - R_i^2)R_a^2}$$

Equation 6.6

where ω is the rotational speed of the inner cylinder, R_i is the inner cylinder radius, R_o is the outer cylinder radius, and R_a is the average radius of both cylinders. The shear rate will be determined through the device geometry and the speed of the motor. Greases that show a shear thinning behavior typically follow a power law equation in regards to the shear stress and viscosity. More specifically, the analysis will follow a Hershel-Bulkley rheological model. For this model, the shear stress has the form:

$$\tau_{\theta r} = \tau_o + k(\dot{\gamma})^n$$

Equation 6.7

where τ_o represents a yield stress, *k* is a consistency factor, and *n* is the flow index [103]. For the rotating cylinder device, the speed of the inner tube can be controlled and maintained at a constant rate. For this experiment, the inner tube was set to rotate at 50 revolutions per minute (RPM) for one minute to establish a consistent shearing of the grease mixture. The shear rate was found to be 128.17^{s-1}. The average shear stress on the petroleum jelly and NP mixture within the annular gap of the concentric cylinders was found to be 136.15Pa.

6.5 Synchrotron micro tomography

Synchrotron-based μ-XCT was conducted at beamline 8.3.2 of the Advanced Light Source (ALS), at Lawrence Berkeley National Laboratory (LBNL). For the NCS-30 + 2.3wt% Fe3O4 grease mixture (Group 2 of Table 3.4), the samples were imaged at 6.9 keV and 7.2 keV, which straddles the K-edge of iron. For the petroleum jelly + 2.3wt% α-ZrP grease mixture (Group 4 of Table 3.4), the samples were scanned at 17.8 keV and 18.2 keV, which straddles the K-edge of zirconium. For all samples, the detection was done with a LuAG:Ce scintillator, and PCO_Edge scientific CMOS camera. Due to the different configurations of the concentric cylinders, the sample sets were imaged using a different magnification. The NCS-30 mixture was imaged using a 2x optical lens, resulting in a pixel size of 0.00319 mm. The petroleum jelly mixture was imaged with a 5x optical lens, resulting in a pixel size of 0.00129. The two dimensional

(2D) orthogonal views of the grease were reconstructed through use of a commercial available imaging processing software package (Octopus) using a Fourier method. To gain a better understanding of the additive distribution within all grease samples, the 2D orthogonal slices were stacked to create a 3D visualization. The 3D reconstruction was accomplished using imaging software called Avizo (FEI Company).

6.6 Tomography results and discussion

The dual-energy computed tomography method, as mentioned before, has been proven to be an effective imaging procedure that can identify a wide variety of chemical compounds. Individual chemical elements are readily identified through analysis of the mass attenuation coefficient. The mass attenuation coefficient for a given element will shift when exposed to two different radiation energies: one energy above and one energy below the K-edge of the given element being sought.

The use of concentric plastic tubes proved to be an effective method to image a grease compound with additives [104]. Based on the results of the previous study, a more rigid and controlled device was constructed to hold and shear grease samples. Using the same dual energy scanning method as before, a sample of petroleum jelly + 2.3wt% α-ZrP nanoparticles was analyzed. As shown in Figure 39, the mass attenuation coefficient of the zirconium in the additive α-ZrP particles exhibits a sharp increase. This effect occurred when the x-ray scanning energies were switched from 17.8 keV to 18.2 keV, which are below and above the zirconium K-edge (17.998 keV). Other detected elements, such as carbon found in petroleum jelly, were shown to have a small decrease in the mass attenuation coefficient across the same energy scanning range. Therefore, the

additives in the petroleum jelly are clearly distinguishable from the bulk. The absorption coefficient related to each of the scanned elements of the synchrotron x-ray are represented by the pixel values within the reconstructed image datasets.

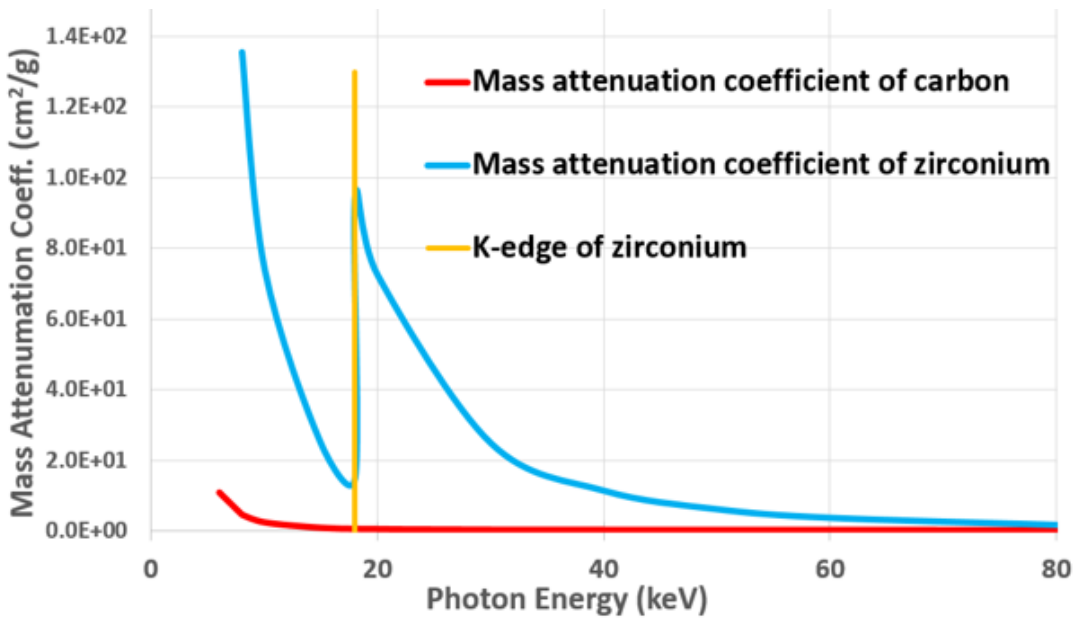

Figure 39. Plot of the mass attenuation coefficient for zirconium (Zr) and carbon (C). The values for all elements were derived from the National Institute of Standards and Technology (NIST) database for X-Ray attenuation.

To observe the α-ZrP nanoparticles, the petroleum jelly + 2.3%wt α-ZrP was radiated before and after a controlled shear force was applied. The respective pixel value distribution is shown in Figure 40. The solid line represents the samples after shear and the dashed line represents the sample before the shear force was applied. After shear, the aggregated α-ZrP additive distributed more uniformly within the annular gap, which will

reduce the concentration of the additive overall. The pixel value/absorption coefficient is reduced after shear as well. Comparing the dual energies, above (red) and below (green) the Zr K-edge, the above K-edge datasets have more counts at the same pixel value and higher overall pixel values than the below K-edge datasets. This trend was seen for both grease samples mixed with the α-ZrP additive.

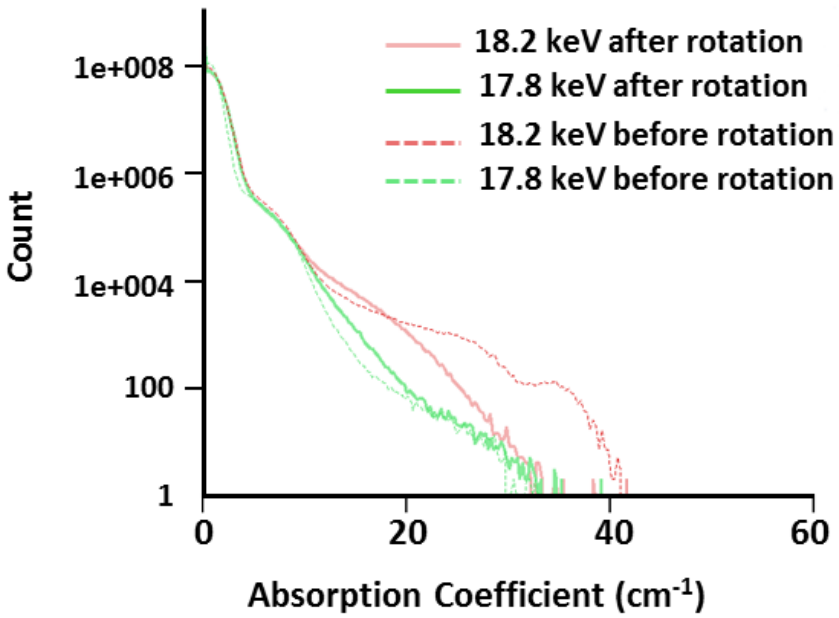

Figure 40. The absorption coefficient distribution of datasets.

Further study was conducted on pure petroleum jelly. This compound contains a combination of different carbon backbones of various chain lengths. As shown in Figure 39, the mass attenuation coefficient of carbon is much less than that of zirconium.

Hence, by adjusting the image color-map, the α-ZrP additive can be clearly distinguished from the petroleum jelly. The results are shown in Figure 41. Figure 41a and Figure 41b show the top view of a 3D visualization for the samples before and after shearing, respectively. Each sample scanned at 18.2 keV. Based on the same colormap, the voxel values of the datasets before shear (Figure 41a) are higher than that after shearing (Figure 41b). This indicates that the additives were randomly aggregated within the annular gap before shearing was applied. Once a shear force was applied, the α-ZrP additives in the samples became more evenly distributed throughout the annular gap of the concentric tubes. Figure 41c and Figure 41d show the cross-sectional view of the each sample. Figure 41e and Figure 41f shows the distribution of α-ZrP additives before and after shear. The imaging clearly shows that the distribution of α-ZrP additives becomes more uniform after a shear force is applied.

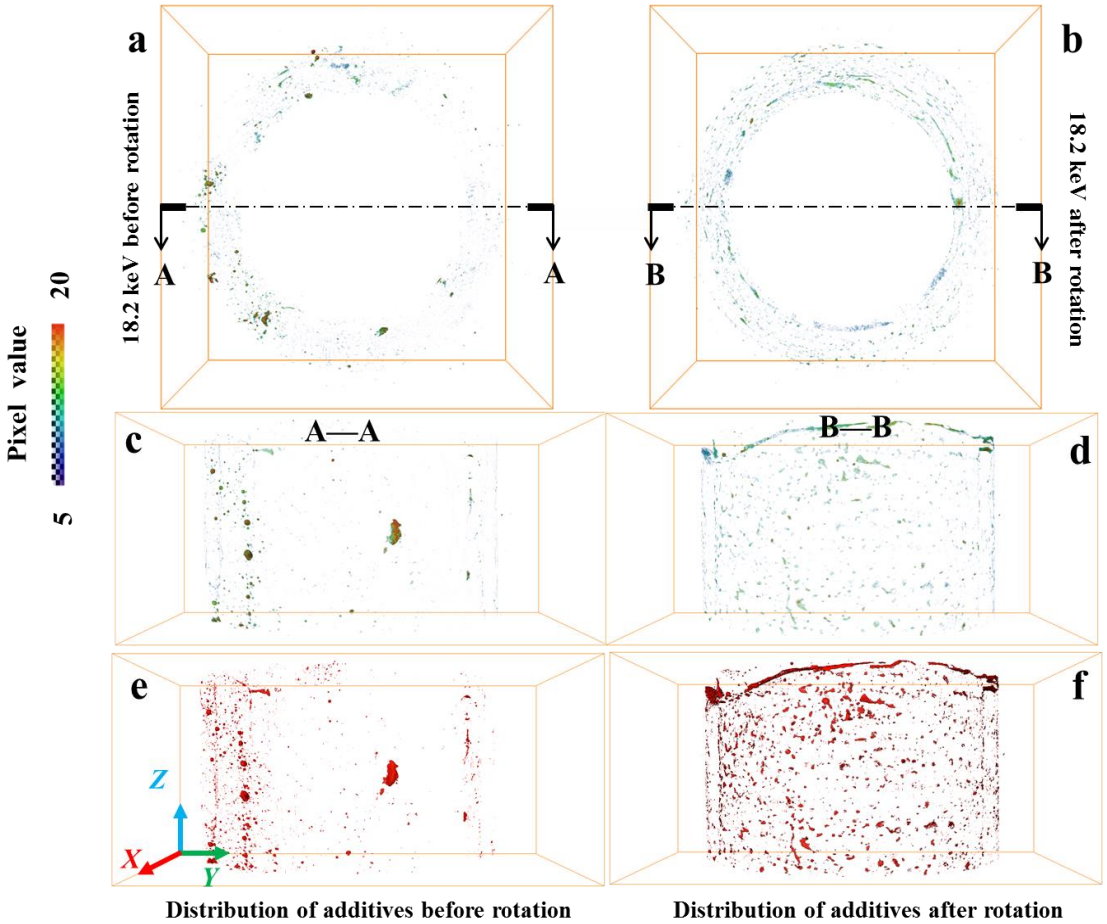

Figure 41. The top view of 3D visualization for group 2 built by 18.2 keV datasets (a) before rotation, (b) after rotation. (c-d) The side sectional view corresponding to the (a-b). The distribution of α-ZrP additives (e) before rotation and (f) after rotation. The box size is 1.7x3.3x1.5 mm.

Through the use of computed tomography, the motion of particle additives in grease may be observed to further support the result of friction testing. As shown with the friction results of the petroleum jelly grease mixtures, the friction coefficient tended to decrease with the addition of α-ZrP nanoparticles. This tendency is supported by previous studies showing that the addition of the zirconium phosphate nanoparticles

decreased the friction and wear of materials when added to a base oil [80]. The mechanism to explain this behavior is that the two dimensional platelet shape of the particles, combined with weak Van der Waals forces holding them together, allow for easy separation under shear. In addition, the platelet structure of the particle lends to the load carrying capability of the lubricant. This theory is confirmed through the tomography imaging of the petroleum jelly + 2.3wt% α-ZrP under shear. The behavior of the particles, and a more concrete visualization of the images in Figure 41, is shown in Figure 42.

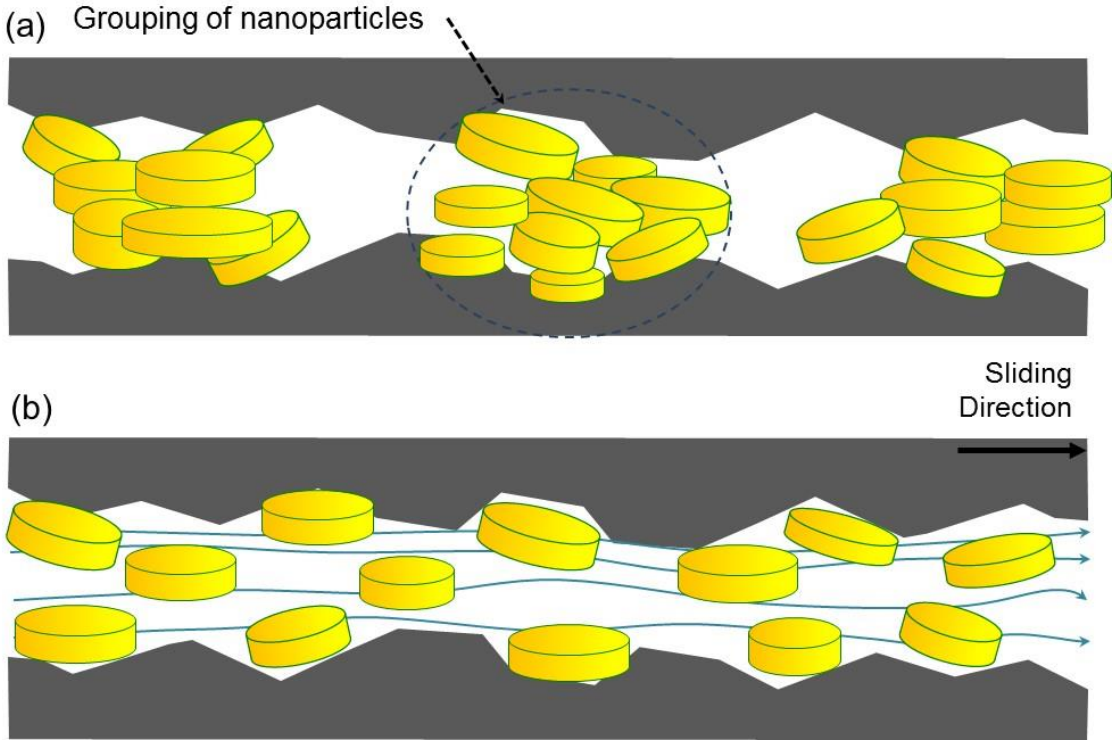

Figure 42. Visual representation of the behavior of the α-ZrP nanoparticles (a) as received, and (b) after a shear stress is applied to the system.

As the figure shows, the nanoparticles will tend to group together if they are not properly mixed. However, once a shear stress is applied, they will readily exfoliate and re-distribute throughout the base grease. The results presented herein show that α-ZrP nanoparticles are a good candidate to enhance the lubricating properties of a grease.

6.7 Significance of *in situ* results

In summary, this research represents the first time that the distribution of inorganic particle additives in a lubricating grease were observed through use of synchrotron-based dual-energy micro computed tomography. It was observed that, as a result of shearing, Fe_3O_4 particles tended to become attached to the edge of the calcium complex thickeners of the base grease and the grease formed a film along the walls of the tubes. A thinner film thickness due to sliding showed higher density overall. This is significant because based on the results, a relationship between a shear force and film thickness could be established *in situ*.

The distribution of particulate additives in petroleum jelly + 2.3wt% α-ZrP nanoparticles was visualized using a more precise concentric tube configuration. Through the use of dual energy K-edge tomography technique, the zirconium element in the particles was distinguishable from the carbon chains comprising the base petroleum jelly grease. Identifying different species within the petroleum jelly mixture allowed for an image mapping of the particulate movement before and after a shear force was applied. The images of the simply mixed petroleum jelly and NPs showed that the particles aggregated in certain areas, a non-homogenous compound. Under the influence

of shear, however, it was observed that the α-ZrP nanoparticles will tend to separate and re-distribute within the annular gap, becoming homogenized. This behavior lends to the reduction in friction coefficient that was reported for petroleum jelly when α-ZrP nanoparticles are added. This research discovered the effectiveness of shear-induced homogeneity of nanoparticles that shed light on low-cost manufacturing of lubricants. In addition, this work opens avenue for future investigations in mechanisms of lubrication.

CHAPTER VII

CONCLUSIONS AND FUTURE RECOMMENDATIONS

7.1 Conclusions

New tribotest methodologies were developed to evaluate the frictional performance of lubricating grease. Through testing the grease under different geometries, a wide range of performance was observed. The test configurations were proven to be effective to reveal tribo-perofrmance and lubrication principles. This research reveals that no matter what contact conditions and geometries a great is being tested, there is a shape factor, $Area = \frac{2P}{3F}$, that can be used to express the contact pressure and friction coefficient. With this factor, it is possible that various testing methods can be unified for comparative study. In addition, fundamental investigation indicates that particular additives into grease can be dispersed effectively during application. This was observed using an in situ tomography method.

This indicated that the mixing process for grease additives, though critical, does not require as much attention for certain additives such as zirconium phosphate. This result indicates that mixing procedures may be reduced, which will greatly improve the efficiency of the manufacturing of grease.

7.2 Future recommendations

The results presented throughout this research represent just a small sampling of lubricating greases and additives. Therefore, it is recommended that more greases and

additives be evaluated using the same methodologies to further expand lubrication studies. Likewise, the newly developed in situ method have several area of improvement. The viscometer device, for example, will need to be equipped with sensors so that stresses may be measured in real time as opposed to calculated after the fact. Additionally, it would be interesting to observe the effects of shear on multiple additives at a time.

REFERENCES

1. Dowson, D., *History of Tribology*. 2 ed. 1998, London, UK: Professional Engineering Publishing.

2. Holmberg, K., P. Andersson, and A. Erdemir, *Global Energy Consumption Due to Friction in Passenger Cars.* Tribology International, 2012. **47**: p. 221-234.

3. Holmberg, K., et al., *Global Energy Consumption Due to Friction in Trucks and Buses.* Tribology International, 2014. **78**: p. 94-114.

4. Hutchings, I.M., *Leonardo Da Vinci'S Studies of Friction.* Wear, 2016. **360-361**: p. 51-66.

5. Kajdas, C., S.S.K. Harvey, and E. Wilusz, *Encyclopedia of Tribology*. Tribology Series: 15. 1990, Amsterdam, NY: Elsevier.

6. Bhushan, B., *Fundamentals of Tribology and Bridging the Gapp between the Macro- and Micro/Nanoscales*, in *Nato science series, series II: mathematics, physics and chemistry*. 2001, SpringerLink: Netherlands.

7. Cameron, A. and C.M.M. Ettles, *Basic Lubrication Theory*. 3rd ed. Ellis Horwood Series in Engineering Science. 1981, New York, NY: E. Horwood

8. Aggarwal, B.B., T.M. Yonushonis, and R.L. Bovenkerk, *Solid Lubrication Design Methodology*. Nasa Contractor Report: 174690. 1984, Cleveland, OH: National Aeronautics and Space Administration, Lewis Research Center.

9. Ghosh, M.K., B.C. Majumdar, and M. Sarangi, *Fundamentals of Fluid Film Lubrication*. 2014, New York, NY: McGraw-Hill Education

10. Vengudusamy, B., et al., *Film Forming Behavior of Greases under Starved and Fully Flooded Ehl Conditions.* Tribology Transactions, 2016. **59**(1): p. 62-71.

11. Cen, H., P.M. Lugt, and G. Morales-Espejel, *Film Thickness of Mechanically Worked Lubricating Grease at Very Low Speeds.* Tribology Transactions, 2014. **57**(6): p. 1066-1071.

12. Cousseau, T., et al., *Friction Torque in Grease Lubricated Thrust Ball Bearings.* Tribology International, 2011. **44**(5): p. 523-531.

13. Cousseau, T., et al., *Influence of Grease Rheology on Thrust Ball Bearings Friction Torque.* Tribology International, 2012. **46**(1): p. 106-113.

14. Svoboda, P., et al., *Study of Grease Behaviour in a Starved Elastohydrodynamically Lubricated Contact.* MM Science Journal, 2014: p. 463-468.

15. Berthe, L., A. Adams-Chaves, and A.A. Lubrecht, *Friction Measurement Indicating the Transition between Fully Flooded and Starved Regimes in Elasto-Hydrodynamic Lubrication.* Journal of Engineering Tribology 2014. **228**(12): p. 1403-1409.

16. Svoboda, P., et al., *Study of Scale Effect in a Starved Elastohydrodynamically Lubricated Contact.* Applied Mechanics & Materials, 2016. **821**: p. 138-143.

17. Srtribeck, R., *Ball Bearings for Any Stress.* Zeitschrift des Vereines Deutscher Ingenieure, 1901. **45**.

18. Stribeck, R., *Characteristics of Plain and Roller Bearings.* Zeitschrift des Vereines Deutscher Ingenieure, 1902. **46**.

19. Szeri, A.Z., *Fluid Film Lubrication* 2nd. ed. 2011, Cambridge, NY: Cambridge University Press.

20. Jao, H.-C., et al., *A Lubrication Theory for Anisotropic Slips and Flow Rheology.* Tribology Transactions, 2016. **59**(2): p. 252-266.

21. Miettinen, J., P. Andersson, and V. Wikström, *Analysis of Grease Lubrication of a Ball Bearing Using Acoustic Emission Measurement.* Proceedings of the

Institution of Mechanical Engineers -- Part J -- Journal of Engineering Tribology (Professional Engineering Publishing), 2001. **215**(6): p. 535-544.

22. Zaretsky, E.V., *Bearing Elastohydrodynamic Lubrication : A Complex Calculation Made Simple*. Nasa Technical Memorandum: 102575. 1990, Washington, DC: National Aeronautics and Space Administration.

23. Schritz, B., *Parched Elastohydrodynamic Lubrication : Instrumentation and Procedure*. Nasa Technical Memorandum: 104426. 1991, Washington, DC: National Aeronautics and Space Administration.

24. Bonneau, D., A. Fatu, and D. Souchet, *Hydrodynamic Bearings*. Numerical Methods in Engineering Series. 2014, London, UK: International Society for Technology in Education.

25. Suetsugu, Y., et al., *Basic Study of Grease Rheology and Correlation with Grease Properties.* Tribology Online, 2013. **8**(1): p. 83-89.

26. Van Rensselar, J., *Grease Particle Evaluation.* Tribology & Lubrication Technology, 2015. **71**(9): p. 32-36.

27. Czarny, R. and M. Paszkowski, *The Influence of Graphite Solid Additives, Mos2 and Ptfe on Changes in Shear Stress Values in Lubricating Greases.* Journal of Synthetic Lubrication, 2007. **24**(1): p. 19-29.

28. Shen, T., et al., *Mechanical Stability and Rheology of Lithium-Calcium-Based Grease Containing Zddp.* RSC Advances, 2016. **6**(14): p. 11637-11647.

29. Drabik, J. and M. Trzos, *Improvement of the Resistance to Oxidation of the Ecological Greases by the Additives.* Journal of Thermal Analysis & Calorimetry, 2013. **113**(1): p. 357-363.

30. Gonçalves, D., et al., *Film Thickness and Friction Behaviour of Thermally Aged Lubricating Greases.* Tribology International, 2016.

31. Chul, H., et al., *Grease Degradation in Constant Velocity (Cv) Joints.* Tribology & Lubrication Technology, 2012. **68**(5): p. 44-51.

32. Rudnick, L.R., *Synthetics, Mineral Oils, and Bio-Based Lubricants : Chemistry and Technology*. 2nd. ed. Chemical Industries: 135. 2013, Boca Raton, FL: CRC Press.

33. Cann, P.M., et al., *Grease Degradation in R0f Bearing Tests.* Tribology Transactions, 2007. **50**(2): p. 187-197.

34. Pan, J.B., Y.H. Cheng, and J.Y. Yang, *Effect of Heat Treatment on the Lubricating Properties of Lithium Lubricating Grease.* Royal Society of Chemistry, 2015. **5**(72): p. 58686-58693.

35. ASTM, *Standard Test Method for Wear Testing with a Pin-on-Disk Apparatus*. 2016, ASTM International: West Conshohocken, PA.

36. Tsai, P.-H. and H.-Y. Chu, *Effects of the Nano-Diamond Additives on the Tribological Performance Improvement of Lubricating Grease.* Key Engineering Materials, 2015. **642**: p. 298-302.

37. Nehme, G., *The Importance of Variable Speeds under Extreme Pressure Loading in Molybdenum Disulfide Greases Using Four-Ball Wear Tests.* Tribology Transactions, 2013. **56**(6): p. 977-985.

38. Gonçalves, D., et al., *Friction Torque in Thrust Ball Bearings Lubricated with Polymer Greases of Different Thickener Content.* Tribology International, 2016. **96**: p. 87-96.

39. Neurouth, A., et al., *Thermal Modeling of a Grease Lubricated Thrust Ball Bearing.* Proceedings of the Institution of Mechanical Enginers - Part J-Journal of Engineering Tribology, 2014. **228**(11): p. 1266-1275.

40. Lugt, P.M., *A Review on Grease Lubrication in Rolling Bearings.* Tribology & Lubrication Technology, 2010. **66**(7): p. 44-56.

41. Cousseau, T., et al., *Film Thickness in a Ball-on-Disc Contact Lubricated with Greases, Bleed Oils and Base Oils.* Tribology International, 2012. **53**: p. 53-60.

42. Bowden, F.P. and D. Tabor, *Friction and Lubrication*. Methuen's Monographs on Physical Subjects. 1956, New York, NY: Wiley.

43. Szeri, A.Z., *Fluid Film Lubrication : Theory and Design*. 1998, Cambridge, NY: Cambridge University Press.

44. Quan, X., et al., *Friction and Wear Performance of Dual Lubrication Systems Combining Ws2–Mos2 Composite Film and Low Volatility Oils under Vacuum Condition.* Tribology International, 2016. **99**: p. 57-66.

45. Gohar, R. and H. Rahnejat, *Fundamentals of Tribology*. 2008, London, UK: Imperial College Press.

46. Rodrigues, A.C.P., et al., *Pin-on-Disc Tribotests with the Addition of Cu Particles as an Interfacial Media: Characterization of Disc Tribosurfaces Using Sem-Fib Techniques.* Tribology International, 2016. **100**: p. 351-359.

47. Djoufack, M.H., et al., *Wear Behaviour of Hydrogenated Dlc in a Pin-on-Disc Model Test under Lubrication with Different Diesel Fuel Types.* Tribology International, 2015. **92**: p. 12-20.

48. Kudish, I., *Asymptotic Methods and Relationships Relevant to Elastohydrodynamic Lubrication Theory*, in *Elastohydrodynamic Lubrication for Line and Point Contacts*. 2013, CRC Press: Boca Raton, FL. p. 29-31.

49. Johnson, K.L., *Contact Mechanics*. 1985, New York, NY: Cambridge University Press. 452.

50. Raous, M., M. Jean, and J.J. Moreau, *Contact Mechanics*. 1995, New York: Springer Science

51. Goryacheva, I.G., *Friction in Sliding/Rolling Contact*, in *Contact Mechanics in Tribology*. 1998, Springer Netherlands: Dordrecht. p. 61-100.

52. Renouf, M., et al., *Numerical Tribology of a Dry Contact.* Tribology International, 2011. **44**(7–8): p. 834-844.

53. ASTM, *Standard Test Method for Determination of the Coefficient of Friction of Lubricants Using the Four-Ball Wear Test Machine*. 2016, ASTM International: West Conshohocken, PA.

54. Neurouth, A., et al., *Thermal Modeling of a Grease Lubricated Thrust Ball Bearing.* Proceedings of the Institution of Mechanical Engineers - Part J- Journal of Engineering Tribology, 2014. **228**(11): p. 1266-1275.

55. Brangetto, M., *Field Hydraulic Tests Improve Hpht Drilling Safety and Performance.* SPE Drilling & Completion, 1999. **14**(4).

56. Xu, J. and Z. Wu, *Tubular String Buckling Theoretical Analysis*, in *Tubular String Characterization in High Temperature High Pressure Oil and Gas Wells*. 2015, CRC Press. p. 19-52.

57. Xu, J. and Z. Wu, *Mechanical Analysis for the Placement of the Test String*, in *Tubular String Characterization in High Temperature High Pressure Oil and Gas Wells*. 2015, CRC Press. p. 53-60.

58. API, *Recommended Practice for Testing of Thread Compound for Rotary Shouldered Connections*. 1992/R2005, American Petroleum Institute: Washington, DC.

59. Karlsson, P., et al., *Galling Resistance and Wear Mechanisms for Cold-Work Tool Steels in Lubricated Sliding against High Strength Stainless Steel Sheets.* Wear, 2012. **286–287**: p. 92-97.

60. van der Heide, E. and D.J. Schipper, *Galling Initiation Due to Frictional Heating.* Wear, 2003. **254**(11): p. 1127-1133.

61. van der Heide, E., A.J. Huis in ‘t Veld, and D.J. Schipper, *The Effect of Lubricant Selection on Galling in a Model Wear Test.* Wear, 2001. **251**(1–12): p. 973-979.

62. Eriksson, J. and M. Olsson, *Tribological Testing of Commercial Crn, (Ti,Al)N and Crc/C Pvd Coatings - Evaluation of Galling and Wear Characteristics against Different High Strength Steels.* Surface and Coatings Technology, 2011. **205**(16): p. 4045-4051.

63. ASTM, *Standard Test Method for Galling Resistance of Materials*. 2009, ASTM International: West Conshohocken, PA.

64. Smith, J.E., *Testing Thread Compounds for Rotary-Shouldered Connections.* SPE Drilling & Completion, 1993. **8**(03): p. 170-174.

65. Baragetti, S. and A. Baryshnikov, *Rotary Shouldered Thread Connections: Working Limits under Combined Static Loading.* Journal of Mechanical Design, 2000. **123**(3): p. 456-463.

66. McDonald, H.B. and C. Bestolife, *Thread Compounds + Environment = Change.* Journal of Petroleum Technology, 1993. **45**(7): p. 614-616.

67. Carper, H.J., *Rating Thread Compounds for Galling Resistance.* Journal of tribology, 1995. **117**(4): p. 639-645.

68. Jatti, V.S. and T.P. Singh, *Copper Oxide Nano-Particles as Friction-Reduction and Anti-Wear Additives in Lubricating Oil.* Journal of Mechanical Science and Technology, 2015. **29**(2): p. 793-798.

69. Gorbatchev, O., et al., *Friction Reduction Efficiency of Organic Mo-Containing Fm Additives Associated to Zddp for Steel and Carbon-Based Contacts.* Tribology International, 2016. **99**: p. 278-288.

70. Wan, S., et al., *An Overview of Inorganic Polymer as Potential Lubricant Additive for High Temperature Tribology.* Tribology International, 2016. **102**: p. 620-635.

71. Nan, F., et al., *Tribological Behaviors and Wear Mechanisms of Ultrafine Magnesium Aluminum Silicate Powders as Lubricant Additive.* Tribology International, 2015. **81**: p. 199-208.

72. Zolotov, A., et al., *A Composition of Organic Hetero Compounds as an Antioxidant and Antiwear Additive for Mineral Lubricating Oils.* Petroleum Chemistry, 2013. **53**(4): p. 262-266.

73. Pawlak, Z., *Tribochemistry of Lubricating Oils*. Tribology and Interface Engineering Series: 45. 2003, Amsterdam: Elsevier.

74. Minfray, C., et al., *Experimental and Molecular Dynamics Simulations of Tribochemical Reactions with Zddp: Zinc Phosphate-Iron Oxide Reaction.* Tribology Transactions, 2008. **51**(5): p. 589-601.

75. Costa, R.P.C., et al., *Tribological Effect of Iron Oxide Residual on the Dlc Film Surface under Seawater and Saline Solutions.* Surface Science, 2011. **605**(7–8): p. 783-787.

76. API, *Recommended Practice on Thread Compounds for Casing, Tubing, and Line Pipe*. 2003/R2015, API: Washington, DC.

77. Robinson, T., H. Ou, and C.G. Armstrong, *Study on Ring Compression Test Using Physical Modelling and Fe Simulation.* Journal of Materials Processing Technology, 2004. **153–154**: p. 54-59.

78. Oganesova, E., et al., *Synthesis of Tungsten Sulfide Nanoparticles and Their Tribological Properties as Additives for Lubricating Oils.* Nanotechnologies in Russia, 2016. **11**(5): p. 312.

79. Park, E.K. and K.W. Song, *Rheological Evaluation of Petroleum Jelly as a Base Material in Ointment and Cream Formulations: Steady Shear Flow Behavior.* Archives of Pharmacal Research, 2010. **33**(1): p. 141-150.

80. He, X., et al., *A-Zirconium Phosphate Nanoplatelets as Lubricant Additives.* Colloids and Surfaces A: Physicochemical and Engineering Aspects, 2014. **452**: p. 32-38.

81. Shuai, M., et al., *Hydrothermal Synthesis of Layered A-Zirconium Phosphate Disks: Control of Aspect Ratio and Polydispersity for Nano-Architecture.* CrystEngComm, 2013. **15**(10): p. 1970-1977.

82. Tang, M., *A Brief Review on A-Zirconium Phosphate Intercalation Compounds and Nano-Composites.* Science in China. Series E, Technological Sciences, 2016. **59**(3): p. 436-441.

83. Snoeijer, J.H., J. Eggers, and C.H. Venner, *Similarity Theory of Lubricated Hertzian Contacts.* Physics of Fluids, 2013. **25**(10): p. 1-6.

84. Tipei, N., *Theory of Lubrication : With Applications to Liquid- and Gas-Film Lubrication*, ed. W.A. Gross. 1962, Stanford, CA: Stanford University Press.

85. Zeng, Q. and G. Dong, *Influence of Load and Sliding Speed on Super-Low Friction of Nitinol 60 Alloy under Castor Oil Lubrication.* Tribology Letters, 2013. **52**(1): p. 47-55.

86. Lugt, P.M., *Grease Lubrication in Rolling Bearings*. Tribology Series. 2013, West Sussex, UK: John Wiley & Sons.

87. Gonçalves, D., et al., *On the Friction Behaviour of Polymer Greases.* Tribology International, 2016. **93**(A): p. 399-410.

88. De Laurentis, N., et al., *The Influence of Bearing Grease Composition on Friction in Rolling/Sliding Concentrated Contacts.* Tribology International, 2016. **94**: p. 624-632.

89. Johnson, P.W., *Classical Mechanics with Applications*. 2010, Hackensack, NJ: World Scientific Publishing Company.

90. Rodriguez-Tembleque, L. and M.H. Aliabadi, *Wear and Contact Mechanics*. Key Engineering Materials. 2014, Durnten-Zurich, Switzerland: Trans Tech Publications, Ltd.

91. Bongaerts, J.H.H., et al., *In Situ Confocal Raman Spectroscopy of Lubricants in a Soft Elastohydrodynamic Tribological Contact.* Journal of Applied Physics, 2008. **104**(1): p. 014913.

92. Shaohua, Z., L. Yuhong, and L. Jianbin, *In Situ Observation of the Molecular Ordering in the Lubricating Point Contact Area.* Journal of Applied Physics, 2014. **116**(1): p. 1-6.

93. Murr, P.J., et al., *Optical Measurement Method for High-Speed Quality Control of Viscous Materials Based on Fluorescence.* Tribology International, 2016. **94**: p. 323-328.

94. Hsieh, J., *Computed Tomography : Principles, Design, Artifacts, and Recent Advances*. 3rd. ed. Spie Press Monograph: Pm259. 2015, Bellingham, WA: SPIE.

95. Scott, A.E., et al., *Three Dimensional Imaging of Paraffin Embedded Human Lung Tissue Samples by Micro-Computed Tomography.* PloS One, 2015. **10**(6): p. 1-8.

96. Xu, X., et al., *Using Micro-Computed Tomography to Evaluate the Dynamics of Orthodontically Induced Root Resorption Repair in a Rat Model.* PLoS ONE, 2016. **11**(3): p. 1-13.

97. Nouri, H., S. Guessasma, and S. Belhabib, *Structural Imperfections in Additive Manufacturing Perceived from the X-Ray Micro-Tomography Perspective.* Journal of Materials Processing Technology, 2016. **234**: p. 113-124.

98. Biziks, V., et al., *Assessment of Wood Microstructural Changes after One-Stage Thermo-Hydro Treatment (Tht) by Micro X-Ray Computed Tomography.* Holzforschung: International Journal of the Biology, Chemistry, Physics, & Technology of Wood, 2016. **70**(2): p. 167-177.

99. Chen, Y., et al., *Observation of Two-Dimensional Yttrium Oxide Nanoparticles in Mealworm Beetles (Tenebrio Molitor).* Journal of Synchrotron Radiation, 2016. **23**(5): p. 1197-1201.

100. Chen, Y., et al., *Observation of Yttrium Oxide Nanoparticles in Cabbage (Brassica Oleracea) through Dual Energy K-Edge Subtraction Imaging.* Journal of Nanobiotechnology, 2016. **14**(1): p. 1-10.

101. He, X., et al., *Two-Dimensional Nanostructured Y2o3 Particles for Viscosity Modification.* Applied Physics Letters, 2014. **104**(16): p. 1-5.

102. Lacaze, L., A. Filella, and O. Thual, *Steady and Unsteady Shear Flows of a Viscoplastic Fluid in a Cylindrical Couette Cell.* Journal of Non-Newtonian Fluid Mechanics, 2015. **220**: p. 126-136.

103. Al-Zahrani, S.M., *A Generalized Rheological Model for Shear Thinning Fluids.* Journal of Petroleum Science and Engineering, 1997. **17**(3): p. 211-215.

104. Chen, Y., et al., *Direct Observation of Lubricant Additives Using Tomography Techniques.* Applied Physics Letters, 2016. **109**(4): p. 1-5.